

Deep Swift/UVOT Observations of GOODS-N and the Evolution of the Ultraviolet Luminosity Function at $0.2 < z < 1.2$

ALEXANDER BELLES,¹ CARYL GRONWALL,^{1,2} MICHAEL H. SIEGEL,¹ ROBIN CIARDULLO,^{1,2} AND MAT J. PAGE³

¹*Department of Astronomy & Astrophysics, The Pennsylvania State University, University Park, PA 16802*

²*Institute for Gravitation and the Cosmos, The Pennsylvania State University, University Park, PA 16802*

³*University College London, Mullard Space Science Laboratory, Holmbury St. Mary, Dorking, RH5 6NT, UK*

ABSTRACT

We present Swift Ultraviolet Optical Telescope (UVOT) observations of the deep field GOODS-N in four near-UV filters. A catalog of detected galaxies is reported, which will be used to explore galaxy evolution using ultraviolet emission. Swift/UVOT observations probe galaxies at $z \lesssim 1.5$ and combine a wide field of view with moderate spatial resolution; these data complement the wide-field observations of GALEX and the deep, high angular resolution observations by HST. Using our catalog of detected galaxies, we calculate the UV galaxy number counts as a function of apparent magnitude and compute the UV luminosity function and its evolution with redshift. From the luminosity function fits in various redshift bins, we calculate the star formation rate density as a function of redshift and find evolution consistent with past works. We explore how different assumptions such as dust attenuation corrections can dramatically change how quickly the corrected star formation rate density changes with redshift. At these low redshifts, we find no trend between UV attenuation and redshift or absolute magnitude with significant scatter in the UV spectral slope β . This dataset will complement the extensive observations of GOODS-N already in the literature.

Keywords: interstellar dust, galaxy evolution, Near ultraviolet astronomy

1. INTRODUCTION

There have been many astrophysical breakthroughs enabled by deep field observations. The original Hubble Deep Field (HDF) found large numbers of high redshift galaxies, providing a glimpse of the early universe (Williams et al. 1996). Many deep field observations followed the success of HDF with larger fields of view and multiwavelength investigations. One such endeavor is CANDELS (Cosmic Assembly Near-infrared Deep Extragalactic Legacy Survey), which observed five separate fields using WFC3 and ACS on the Hubble Space Telescope (HST) (Grogin et al. 2011). One of the CANDELS fields, GOODS-N (Great Observatories Origins Deep Survey North), covers the original HDF and has existing observations from other space based observatories (Giavalisco et al. 2004; Elbaz et al. 2011). Here, we add deep Swift/Ultraviolet Optical Telescope (UVOT)

(Gehrels et al. 2004; Roming et al. 2005) observations of the GOODS-N field to the existing data in the literature. These data will facilitate a number of investigations, including the exploration of the UV galaxy number counts, the evolution of the luminosity function (LF) with redshift, and modeling of the spectral energy distributions (SEDs) of interesting sources such as Lyman Break Galaxies (LBGs). Previous work using deep UVOT imaging of the Chandra Deep Field South (CDF-S) showed the breadth of science possible by these deep near-UV observations (Hoversten et al. 2009; Basu-Zych et al. 2011; Hagen et al. 2015).

Observations of galaxies using the far or near UV directly probe recent star formation. For galaxies at redshifts below 1.5, the rest-frame FUV can only be studied using space-based UV telescopes. HST is the highest angular resolution UV telescope and can reach depths of $m_{AB} \sim 30$ (Illingworth et al. 2013) but is limited by a narrow field of view. This is problematic as galaxy surveys of the high redshift universe must be done over a large area to mitigate the effects of cosmic variance (Somerville et al. 2004). Wide field imaging surveys like

those done by GALEX are not hindered by cosmic variance, but GALEX observations are confusion-limited due to low angular resolution (Xu et al. 2005). Sitting intermediate between these extremes is Swift/UVOT which has a larger field of view ($\sim 17'$) than HST and higher resolution ($\sim 2.5''$) than GALEX. Additionally, UVOT provides more granular wavelength coverage in the near-UV than GALEX. The Ultraviolet Imaging Telescope (UVIT) on the AstroSat observatory occupies a similar niche, with its larger, half degree field of view, sub 2 arcsec spatial resolution, and similar aperture size (37.5 cm) compared to UVOT (Kumar et al. 2012; Tandon et al. 2017; Mondal et al. 2023b). Other studies have used the Optical Monitor (OM) on XMM-Newton to perform similar observations (Mason et al. 2001; Antonucci et al. 2015; Page et al. 2021). The UV emission of galaxies at these redshifts remain valuable as they can be paired with observations across the electromagnetic spectrum to understand the total energy budget of galaxies.

While ultraviolet data of galaxies in this redshift range are scarce, there are extensive datasets available at longer wavelengths. The original Great Observatories Origins Deep Survey combined IR HST imaging, ground-based optical data, Spitzer mid-IR photometry and deep Chandra X-ray observations (Alexander et al. 2003; Giavalisco et al. 2004). The CANDELS survey provides UV through IR data over 5 fields of which deep multiwavelength HST observations exist for ~ 125 square arcminutes of the two GOODS fields (Grogin et al. 2011; Koekemoer et al. 2011). Later HST surveys, such as HDUV (Oesch et al. 2018) and UVCANDELS (Wang et al. 2024), provided additional deeper UV imaging of the GOODS fields, adding to the wealth of data available for these fields. Grism and photometric data also exist from the 3D-HST survey (Skelton et al. 2014; Momcheva et al. 2016).

These multiwavelength data are essential to pair with UV observations. As dust preferentially affects UV radiation, multiwavelength data can be used to model both the stellar populations and the dust properties of the galaxy (for details on modeling the spectral energy distribution of galaxies, see Walcher et al. 2011; Conroy 2013). Additionally, more data across the electromagnetic spectrum improves the precision of photometric redshift estimates, which are necessary to calculate luminosity from observed fluxes (Salvato et al. 2019).

Results from GALEX and HST are essential to our understanding of the UV evolution of galaxies. Observations using GALEX provided a wide-field sample of the UV emission of galaxies at $z \sim 1$, which previously could only be observed with HST. These observations enabled

measurements of the galaxy population over a large area as well as over a large fraction of cosmic time. Xu et al. (2005) studied the FUV and NUV galaxy number counts down to 24.5 AB mag, finding results consistent with an evolving LF. Wyder et al. (2005) determined the LF in the local universe ($z < 0.1$), while Arnouts et al. (2005) and Schiminovich et al. (2005) studied the evolution of the LF and star formation rate density out to $z \sim 1.2$.

Data from HST have been used to study the faintest galaxies. Oesch et al. (2010) traced the evolution of the UV LF in the GOODS-S field at $0.75 < z < 2.5$ using HST and found that at $z \sim 1$, the faint end slope of the luminosity function was steeper than what was found in the local universe. Recent work by Sun et al. (2023) used data from the UVCANDELS project to calculate the evolution of the UV LF in a larger area than past works. Additionally, AstroSat UVIT has produced deep field imaging in the UV to study stellar populations over this redshift range (Bhattacharya et al. 2023; Mondal et al. 2023a,b).

Beyond LF science, these observations allow detailed study of the UV spectral energy distributions of high redshift galaxies, which are highly sensitive to the effects of dust. Overzier et al. (2011) found that high redshift LBGs are consistent with the IRX- β relationship originally derived in Meurer et al. (1999). More work has continued in studying the evolution in the UV spectral slope of galaxies, which is indicative of evolution in the stellar populations as well as dust attenuation properties (Kurczynski et al. 2014). Reddy et al. (2018) probed fainter galaxies at $z \sim 2$, finding that their IRX- β relation is consistent with a Small Magellanic Cloud-like extinction law (Gordon et al. 2003). The finer wavelength resolution provided by Swift/UVOT will be used to understand dust properties at $z \sim 1$.

Previous UVOT work using observations of the Chandra Deep Field South (CDF-S) showed its ability to complement the multiwavelength and other UV data in the literature. Hoversten et al. (2009) showed that the UV number counts were consistent with an evolving LF. Hagen et al. (2015) later quantified the evolution in the Schechter function parameters with redshift (Schechter 1976). These previous works suffered from incompleteness at the faint end of the luminosity function, meaning the faint end slope α was unconstrained (Hagen et al. 2015). Recent works by Page et al. (2021) and Sharma et al. (2022a) using OM, on which UVOT was designed, studied the UV LF in the ROSAT 13h deep field and the CDF-S respectively, with more recent work done on the COSMOS field (Sharma et al. 2022b). Sharma et al. (2022a) found characteristic magnitudes that were about half a magnitude less luminous than those found

by Hagen et al. (2015) for the same field and were able to constrain the faint end slope of the Schechter function. In this work, we will construct a catalog of UVOT detected sources in GOODS-N that will be used in conjunction with data from the literature to further study the redshift evolution of star-forming galaxies. With the additional near-UV coverage provided by UVOT, we will explore correcting the effects of dust attenuation.

Currently, observations by JWST are pushing the boundaries of our knowledge by finding star-forming galaxies at $z \sim 10$ (Curtis-Lake et al. 2023; Robertson et al. 2023). For galaxies at this extreme redshift, JWST probes the rest-frame UV and optical emission. Observations of the rest-frame infrared, which can be used to constrain the effects of dust, are not possible for these objects. JWST is also finding massive red galaxies at $z \sim 8$, raising questions about our cosmological models and theories of galaxy formation Labbé et al. (2023). As we reach to study the first generations of galaxies, it is also imperative to continue to expand our knowledge at lower redshifts where data are more plentiful. These lower redshift results will serve as an important comparison when studying the very early universe.

The paper is laid out as follows: we present our UVOT data in §2, provide our results on the UV number counts and UV luminosity function in Section 3. Finally, we discuss our results in Section 4 and present conclusions in Section 5. Throughout, the AB magnitude system is used (Oke & Gunn 1983) along with a flat Λ CDM cosmology with $h = 0.7$, $\Omega_m = 0.3$ and $\Omega_\Lambda = 0.7$.

2. DATA

Swift observations of GOODS-N (α_{J2000} , $\delta_{J2000} = 189.20^\circ$, 62.2314°) occurred daily throughout 2021. Data were taken using 4 near-UV filters (UVW2, UVM2, UVW1, and u), as well as contemporaneous X-ray observations taken with XRT as part of a Swift Cycle 17 Guest Investigator program (Prop. No.: 1720039). In this Section, we summarize the observations and discuss the data processing procedure.

2.1. UVOT

As the longest continuous observation by Swift is limited to 1.8 ks, many observations of GOODS-N were required to achieve the desired depth. Observations were taken daily from April 1st to December 24th, 2021 in one of the four near UV filters. In total, the field was observed for a total of 80, 78, 80, and 73 ks in the UVW2, UVM2, UVW1, and u filters respectively. The central wavelengths for these filters are 1967, 2260, 2629, and 3469 Å, and the quoted FWHM of the PSF are $2.92''$, $2.45''$, $2.37''$, and $2.37''$. The exposures for each filter

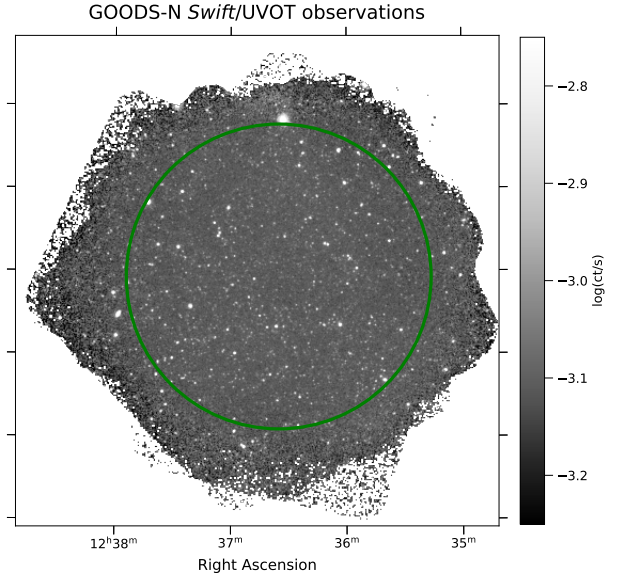


Figure 1. GOODS-N as observed using the Swift/UVOT UVM2 filter. The UVM2 image is shown due to its low background compared to the other filters. The green circle marks the region where we detected the sources presented here. Sources outside this region were excluded due to the lower effective exposure time at the edge of the mosaicked field.

were combined into a single mosaic. UVOT has a field of view of 17 arcminutes and pointing accuracy on the order of 1 arcminute. Combined with roll angle differences, the actual total observed field is slightly larger than expected from the 17 arcminute FOV.

Data were processed in two ways. For each method, we first correct for bad pixels and large scale sensitivity variations across the detector (Siegel et al. 2014). For our first processing method, we sum the counts images and the exposure maps separately using the Heasoft provided tool `uvotimsum`. We then create a total count rate image by dividing the summed counts image by the total exposure map. Due to a variable background between exposures, this method of combining the data led to a non-uniform background in the final count rate image. This was particularly an issue in the u band images, where the background count rate varied by up to a factor of ten between observations, likely due to scattered light from the Earth limb.

To mitigate this, we use the `astropy` (Astropy Collaboration et al. 2013, 2018, 2022) coordinated package `reproject` (Robitaille et al. 2023) to average the count rate images of individual exposures with background matching. The background matching is done by calculating the measured count rate differences of overlapping regions and adding a constant offset to each image

in order to minimize these differences. While the average correction is constrained to be zero, this procedure may add a small offset to our final mosaic. However, this procedure leads to a more uniform background in the final count rate image.

We calculate photometry using both stacking methods. We verify that the standard UVOT point source photometry tool `uvotsource` gives comparable fluxes for both stacking methods. However, we find a more uniform background when combining the u band images using count rate averaging, with no negative impact on the other filters. Therefore, the mean averaged count rate image is used as our mosaicked image for all filters. In Figure 1, we show the UVM2 mosaic image and highlight the outer regions where data were excluded due to lower effective exposure times.

After the final science images were created, sources were identified and photometry measured with Source Extractor (Bertin & Arnouts 1996). First, we create a metaimage that is used for detecting sources and determining the aperture shape and size. Our metaimage is the sum of the count rate images for the UVW2, UVM2, and UVW1 filters. Compared to using a single band, this ensures that we detect sources even if they are not seen in each filter. The u band data are excluded from the metaimage due to the overall higher background level even after our averaging procedure. To best measure the brightest sources as well as identify the faintest objects, we employ a two step approach for Source Extractor (see Galametz et al. 2013; Guo et al. 2013). For the first step (“cold” mode), we identify the brightest sources without aggressively deblending, using similar configuration settings as those described in Hoversten et al. (2009) for CDF-S data. The second mode (“hot” mode) is configured to detect the faintest possible sources. Running SExtractor in cold mode would not split a clumpy galaxy into multiple sources while hot mode would. After running SExtractor in both modes, we combine the sources into one catalog.

All sources detected using the cold mode settings are included in the catalog. For the sources detected in the hot mode, we exclude all hot mode identified sources that fall within the Kron aperture of a cold source. This prevents double counting sources and also prevents bright sources from needlessly being split into multiple sources.

We use the `MAG_AUTO` values from SExtractor, which is based on Kron (1980). `MAG_AUTO` uses a flexible elliptical aperture based on the observed light distribution for each detected source. The zero-points from Breeveld et al. (2010) were used, along with the most

recent time dependent sensitivity loss correction.¹ As the zero-points are defined for a 5 arcsecond aperture, we calculate the radius of the circular aperture equal in area to the Kron aperture and use the curve of growth for the different UVOT bands to correct the fluxes (see Declair et al. 2019).

We test that the photometry using SExtractor is accurate by confirming that that `uvotsource` photometry using a 5 arcsecond aperture agrees with the SExtractor values. We note that the distribution of the difference between the aperture and SExtractor magnitudes is centered around zero with a long tail towards the SExtractor magnitudes being brighter by up to 0.5 mag in some cases. At the same time, the errors on the SExtractor `MAG_AUTO` values were systematically larger.

As UVOT is a photon counting device, coincidence loss occurs when two photons arrive within the 11 ms frametime. However, analyses of the coincidence loss as a function of count rate in Poole et al. (2008) and Breeveld et al. (2010) shows that for the low count rates seen here, the error introduced due to coincidence loss is negligible so we do not apply any coincidence loss correction. Other works such as Hoversten et al. (2009) and Basu-Zych et al. (2011) also found the coincidence loss correction to be on the order of 1%.

2.2. XRT

While UVOT drives our main science, XRT observations of the field occurred simultaneously and can be used to identify X-ray sources such as active galactic nuclei (AGN). However, as this field has also been observed by the Chandra X-ray Observatory for 2 Ms (Xue et al. 2016), deeper X-ray observations exist in the literature. After cross-matching our catalog with the catalog from Yang et al. (2014), we separate out X-ray sources and stellar contaminants.

2.3. Literature Photometry

With the UVOT photometry presented here, we cross match our detected galaxies with catalogs from previous works. We use the catalog from Yang et al. (2014) to cross match with our UVOT detected sources to get photometric redshifts, spectroscopic redshifts when available, object classification (X-ray source or star), as well as photometry in the optical through infrared.

Other catalogs providing photometry and redshift estimates of objects in this field exist. For example, Barro et al. (2019) provides an updated catalog of H-band detected sources. Near-IR data can also be found in Hsu

¹ https://heasarc.gsfc.nasa.gov/docs/heasarc/caldb/swift/docs/uvot/uvotcaldb.throughput_06.pdf

et al. (2019). These other sources of photometry only provide partial coverage of the UVOT observed field of view. Since Yang et al. (2014) covers the entire area imaged by UVOT, it allows the use of self consistent redshift estimates.

To minimize possible source confusion, we set a 1.5 arcsecond tolerance when matching UVOT detected sources to the Yang et al. (2014) catalog. After matching, 56 objects are classified as X-ray sources. Yang et al. (2014) state that the vast majority of X-ray sources are AGN so they are excluded here as they are assumed to not be typical star-forming galaxies.

For our final catalog, roughly 60% of the objects have spectroscopic redshifts. Of those with only photometric

redshifts, greater than 90% of those sources have high quality photometric redshift estimates ($Q_z < 1$, Brammer et al. 2008). Yang et al. (2014) quote a normalized median absolute deviation of 0.026 for non X-ray sources at $z < 1$. They also claim a 3.9% outlier percentage, where an outlier is defined as $|z|/(1 + z_{spec}) < 0.15$. Following the advice of Yang et al. (2014), we make a photometric redshift cut by requiring $Q_z < 1$.

Table 1 contains the UVOT catalog as described. In total, 1171 sources were identified with matching counterparts within 1.5 arcseconds of source in the Yang et al. (2014) catalog. After removing poor photometric redshift estimates and stellar/X-ray sources, we are left with 1011 sources.

Table 1. Catalog of UVOT detected sources in GOODS-N

α (deg)	δ (deg)	UVW2 mag	UVW2 err	UVM2 mag	UVM2 err	UVW1 mag	UVW1 err	u mag	u err
189.1813886	62.3951872	23.54	0.24	24.11	0.48	23.77	0.50	23.93	0.88
189.1994436	62.3946238	23.37	0.24	23.37	0.29	22.73	0.23	22.18	0.21
189.1669418	62.3924013	24.25	0.37	23.26	0.18	22.95	0.19	22.76	0.24
189.228319	62.3895898	22.90	0.21	22.94	0.26	22.63	0.28	22.98	0.59
189.1163935	62.3884952	23.78	0.39	23.24	0.28	22.82	0.27	22.60	0.34
189.1711512	62.3884962	23.60	0.30	23.62	0.36	23.37	0.41	22.91	0.41
189.1524967	62.3848727	23.04	0.22	22.76	0.20	22.77	0.29	22.67	0.40
189.0225393	62.3845391	23.55	0.24	23.65	0.31	23.25	0.31	22.61	0.26

NOTE—Table 1 is published in its entirety in the machine-readable format. A portion is shown here for guidance regarding its form and content.

3. RESULTS

3.1. Bias

Before we can analyze our data, we have to understand its limitations and biases. First, our survey is flux-limited, meaning the data suffer from Malmquist bias, where brighter objects are detected out to farther distances. This means that intrinsically luminous sources can appear to be more numerous as they can be detected in a larger volume than dimmer sources. To account for this bias, we model our completeness as a function of apparent magnitude, i.e. determining the fraction of sources at a given apparent magnitude that can be detected. We calculate this by injecting artificial sources of known flux into the final mosaicked and detection images, running our detection algorithm, and recording if the artificial source was detected. This technique is common throughout the literature (for example,

Smail et al. 1995; Hoversten et al. 2009; Page et al. 2021; Sharma et al. 2022a).

We assume that these galaxies are point sources, described using a Gaussian profile with a FWHM equal to the PSF for the given UVOT filter. Page et al. (2021) found that XMM-Newton OM detected galaxies at $z > 0.6$ were point sources. As UVOT is based on and strongly influenced by OM, we assume that galaxies at the same redshift and magnitude are point-like. Thus we need to confirm that the lowest redshift galaxies at $z \sim 0.2$ are point-like. To do so, we use the Kron radius, which is used to determine the flux of the galaxies, as a measure of their spatial extent. We find that, within the redshift bins $0.2 < z < 0.4$, $0.4 < z < 0.6$, $0.6 < z < 0.8$, and $0.8 < z < 1.2$, the median Kron aperture radius is relatively constant at around 5.5 arcseconds. We see a trend where the aperture size increases for fainter objects. We attribute this to the source count rate approaching the sky background level. This same increasing of aperture size for low count rates happens

for the injected artificial sources. As a result, the signal to noise drops for the faintest objects.

To calculate the completeness as a function of apparent magnitude, we estimate the fraction of recovered sources at discrete magnitude points. As the completeness drops rapidly at a certain level, our intervals are not evenly spaced, with smaller steps in regions where the completeness changes rapidly. At each discrete apparent magnitude point, we generate a single artificial source with a count rate corresponding to that apparent magnitude. To mimic the noise characteristics of our images, we apply Poisson noise based on the number of detected counts. The artificial source is added to both the detection image and the science image. When adding the artificial source to our metaimage, we scale its count rate by a factor of three. As the metaimage is the sum of the count rate images for the UVW2, UVM2, and UVW1 filters, this is roughly equivalent to assuming a constant spectrum in f_ν . After this source is added to the detection image, we run our detection pipeline and record whether the artificial source is detected at its known position. This is repeated 500 times for each discrete apparent magnitude and then for each of the 4 UVOT filters.

For each UVOT filter, we detect $\sim 98\%$ of sources at the bright end and our completeness levels off at $2 - 4\%$ at the faint end. This implies both our confusion bias and spurious sources percentage is on the order of a few percent. This low level of confusion bias is a clear advantage over surveys by GALEX which can have source confusion at the $\sim 20\%$ level (Ly et al. 2009).

Another possible source of error is the inclusion of interlopers such as stars or spurious sources. The purity of our sample is based on the purity of the Yang et al. (2014) catalog as we require each UVOT detected source to have also been detected in Yang et al. (2014). We use their source classification to remove stars and X-ray objects from our sample. They find that for sources with spectroscopy, only 0.4% of galaxies were misclassified as stars and $\sim 10\%$ of stars were misclassified as galaxies. However, these misclassifications were primarily bright sources or blended with a nearby object.

Using the discrete measurements of the completeness fraction as a function of apparent magnitude, we fit the data with the function defined in Fleming et al. (1995),

$$C(f) = \frac{1}{2} \frac{1 + \xi \log(f/f_{50})}{\sqrt{1 + \xi \log(f/f_{50})^2}}, \quad (1)$$

where ξ is a constant and f_{50} is the flux level at 50% completeness. Converting f_{50} to magnitudes, we find that our 50% completeness levels for the UVW2, UVM2, UVW1, and u band are 24.7, 24.66, 24.25, and 23.85

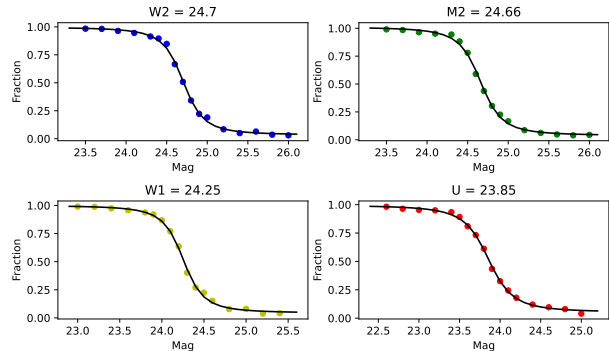


Figure 2. Completeness curves for the four UVOT bands. Detectability is a complex function of exposure time, filter transmission curve, surface brightness, and detection algorithm. We artificially inject point sources of known flux into our images and determine if they are recovered by SExtractor and at what magnitude. This is repeated to build up statistics on the recovery fraction. The completeness curves are shown as well as the magnitude at which our observations are 50% complete.

mag. The results of our completeness simulations can be seen in Figure 2 and the Fleming curve provides an excellent fit.

We perform another test to determine to what extent SExtractor detected sources are impacted by source size. We repeat our detection process where our injected sources have a FWHM equal to twice the PSF. This was only done for the UVM2 filter. We find that the 50% completeness level drops by approximately 0.8 mag, due to the lower surface brightness. We also see that the median Kron aperture size increases. The median aperture size of the point sources was 4.5 arcseconds compared to 7.5 for the extended sources added in this test. This shows that the SExtractor dynamic aperture sizing can detect extended sources by using a larger aperture albeit to a lesser depth. As the average size of the sources detected in our images is comparable to the Gaussian with FWHM equal to the PSF, we conclude that, by and large, the detected sources are compact and not extended. Nonetheless, in the lowest redshift bin ($0.2 < z < 0.4$) it is possible that we are overestimating the completeness at the faintest magnitudes.

Another source of bias was described in Eddington (1913). This so-called Eddington bias is when measurement errors scatter sources into brighter bins. This can affect the luminosity function at the bright end, where the shape of the luminosity function is changing rapidly and only depends on a handful of objects. Here, we only discuss the observed luminosity function without an Eddington bias correction.

The last source of potential error is cosmic variance. Cosmic variance is the inherent statistical uncertainty

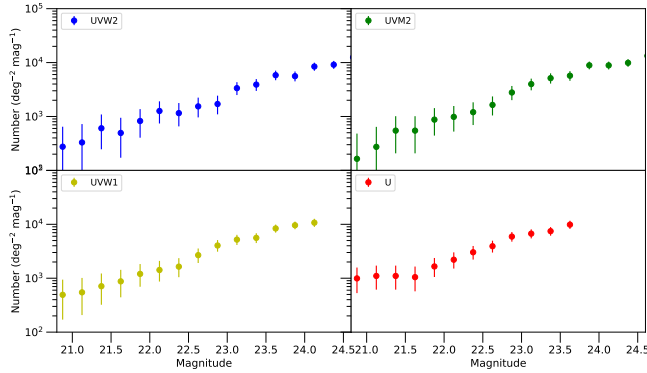


Figure 3. Galaxy number counts as a function of apparent magnitude using Swift/UVOT down to the 50% completeness limit. We bin our sample in steps of 0.25 mag and calculate the number of galaxies detected per square degree per magnitude and corrected for completeness. The error bars are the Poisson noise associated with each bin (Gehrels 1986). We do not increase the error bars to compensate for the effects of cosmic variance.

when observing only one small part of the universe. Due to random statistical fluctuations, observations of one area of sky may be significantly different than another. As a result, the true error on a measurement is larger than the Poisson error. Somerville et al. (2004) quantified the effects of cosmic variance in the GOODS

fields. Additionally, an online calculator is available from Trenti & Stiavelli (2008) to estimate the cosmic variance for given survey parameters. Similar to Hagen et al. (2015), we find that the contribution of cosmic variance is $\sim 2\times$ the Poisson error. As cosmic variance is a systematic effect in density, we do not incorporate its contribution into our quoted error bars.

3.2. Number Counts

We first look at the number counts of galaxies in our four near-UV bands. We note that there is a known overdensity at $z \sim 0.5$ and $z \sim 0.9$ in the HDF-N, which is encompassed by the field observed here (Cohen et al. 2000).

We bin our sample of detected galaxies into intervals of width 0.25 mag. For each bin, the number count is the total number of galaxies at that apparent magnitude divided by the survey area and magnitude bin width. This is finally normalized based on the completion fraction for each bin. The error on the number density of sources is the Poisson error as determined using Gehrels (1986). Our number counts for the four UVOT filters are shown in Figure 3 down to the 50% completeness limit.. The tabulated values are listed in Table 2.

Table 2. Number count data for each of the 4 UVOT filters

Bin center (AB Mag)	Number count ($\text{deg}^{-2} \text{mag}^{-1}$)	Lower limit	Upper limit	N_{raw}	Completeness
20.875	274.978	156.495	460.570	5	0.984
21.125	329.973	199.372	526.659	6	0.984
21.375	604.951	425.603	847.532	11	0.984
21.625	494.960	333.342	720.666	9	0.984
21.875	824.933	614.554	1097.374	15	0.984
22.125	1264.897	1003.265	1587.241	23	0.984
22.375	1154.906	905.100	1465.688	21	0.984
22.625	1539.874	1250.785	1889.143	28	0.984
22.875	1704.861	1400.484	2069.161	31	0.984
23.125	3354.726	2926.500	3841.465	61	0.984
23.375	3904.681	3442.488	4425.130	71	0.984
23.625	5836.939	5270.995	6460.621	106	0.983
23.875	5600.578	5041.556	6218.403	100	0.966
24.125	8444.788	7749.151	9200.241	147	0.942
24.375	9134.446	8394.447	9936.976	152	0.900
24.625	12524.756	11485.959	13653.515	145	0.627
24.875	23192.393	20964.528	25645.327	108	0.252
20.875	163.987	75.015	322.992	3	0.990
21.125	273.311	155.546	457.779	5	0.990
21.375	546.622	376.944	779.544	10	0.990
21.625	546.622	376.944	779.544	10	0.990

Table 2 continued

Table 2 (*continued*)

Bin center (AB Mag)	Number count (deg ⁻² mag ⁻¹)	Lower limit	Upper limit	N_{raw}	Completeness
21.875	874.595	658.466	1152.190	16	0.990
22.125	983.920	754.384	1274.535	18	0.990
22.375	1202.569	948.331	1517.277	22	0.990
22.625	1639.866	1342.313	1997.060	30	0.990
22.875	2787.772	2398.822	3235.207	51	0.990
23.125	3990.341	3524.491	4514.050	73	0.990
23.375	5138.247	4609.321	5724.653	94	0.990
23.625	5706.485	5147.914	6322.614	104	0.986
23.875	8902.615	8197.414	9666.027	159	0.966
24.125	8877.004	8167.118	9646.071	156	0.951
24.375	9888.530	9117.237	10722.472	164	0.897
24.625	13332.825	12191.100	14576.786	136	0.552
24.875	15650.535	13797.998	17736.570	71	0.246
20.875	491.960	331.322	716.299	9	0.990
21.125	546.622	376.944	779.544	10	0.990
21.375	710.609	516.314	967.105	13	0.990
21.625	874.595	658.466	1152.190	16	0.990
21.875	1202.569	948.331	1517.277	22	0.990
22.125	1421.217	1144.474	1757.969	26	0.990
22.375	1639.866	1342.313	1997.060	30	0.990
22.625	2678.448	2297.257	3118.201	49	0.990
22.875	4045.003	3575.957	4571.886	74	0.990
23.125	5199.474	4667.059	5789.427	95	0.989
23.375	5601.510	5045.161	6216.078	101	0.976
23.625	8382.110	7693.967	9129.216	148	0.956
23.875	9599.736	8850.968	10409.322	164	0.924
24.125	10727.597	9840.900	11690.809	146	0.737
24.375	23753.705	21696.864	25996.884	133	0.303
20.875	991.935	760.530	1284.918	18	0.982
21.125	1102.150	857.976	1407.572	20	0.982
21.375	1102.150	857.976	1407.572	20	0.982
21.625	1047.043	809.168	1346.324	19	0.982
21.875	1653.226	1353.248	2013.330	30	0.982
22.125	2204.301	1857.381	2610.677	40	0.982
22.375	3030.913	2623.600	3497.046	55	0.982
22.625	3921.619	3457.421	4444.326	71	0.980
22.875	5917.351	5340.894	6552.911	105	0.960
23.125	6711.128	6094.288	7387.459	118	0.951
23.375	7458.237	6802.518	8174.316	129	0.936
23.625	9857.867	9037.434	10749.609	144	0.791
23.875	10630.856	9536.526	11844.109	94	0.479

NOTE—Data are shown in order for UVW2, UVM2, UVW1, and u . The 1σ upper and lower limits are determined using [Gehrels \(1986\)](#) and we do not correct for cosmic variance.

We compare our number counts to other studies in the literature. We focus on comparing the UVM2 number counts found here for GOODS-N to the UVM2 number counts in CDF-S from [Hoversten et al. \(2009\)](#), the GALEX NUV all-sky number counts from [Xu et al. \(2005\)](#), and the HST FUV number counts from [Teplitz et al. \(2006\)](#). Our focus is on the UVM2 results as the

filter does not suffer from a red leak like the UVW2 and UVW1 filters ([Brown et al. 2010](#); [Siegel et al. 2014](#)) and is most similar to GALEX NUV, minimizing the effects of any assumptions made when applying a color correction to compare the two.

In order to accurately compare the observed UVM2 number counts to that of other filters, specifically the HST FUV number counts, we must determine the color difference between pairs of filters. We assume that a

power law is a reasonable approximation for the spectral energy distribution (SED) in the UV. For each source in our sample, we calculate the slope β that best fits $F(\lambda) \propto \lambda^\beta$ using the UVOT photometry. This is the slope of the observed UV spectrum and not the true rest-frame UV slope. We look at the distribution of the power law slopes and find the median is -0.754 and a mean of -0.473 , implying a long tail towards larger values of β . We use the median $\beta = -0.754$ and calculate the expected UVM2-NUV color for this representative source.

We find that for $\beta = -0.754$, the UVM2-NUV color is -0.018 . This slight color difference is smaller than the Galactic extinction correction. Assuming a reddening of $E(B - V) \sim 0.01$ (Schlegel et al. 1998; Schlafly & Finkbeiner 2011), a Fitzpatrick (1999) extinction law, $R_V = 3.1$, and a flat input spectrum, the correction for the UVM2 filter is 0.09 mag. Changing the flat input spectrum assumption to a spectrum with UV slope $\beta \sim -0.75$ does not meaningfully change the MW extinction correction.

To compare with the Teplitz et al. (2006) FUV number counts, the color correction will be non-negligible and require an assumption of the input spectrum. We assume a power law spectrum of $\beta = -0.754$ and find the difference between the HST F150LP and UVOT UVM2 filter to be -0.274 . This correction is applied to the number counts from Teplitz et al. (2006).

Figure 4 shows the UV number counts here compared to prior works and there is good agreement at the $\sim 10\%$ level. Our values here have larger errors than the Xu et al. (2005) values due to the different survey sizes (266 arcminutes here versus many square degrees in Xu et al. 2005) but our measurements go a magnitude deeper. The CDF-S values from Hoversten et al. (2009) go slightly deeper than the work presented here due to greater exposure time (80 ks here vs ~ 130 ks).

While the more astrophysically interesting quantity is the luminosity function, the number counts can be used to understand the galaxy population when other photometry is not available or the redshifts of objects are unknown. The number counts can be used to test evolution in the galaxy population as was done in Hoversten et al. (2009). As the redshifts for these objects have already been measured or estimated in Yang et al. (2014), we now turn our attention to the UV luminosity function.

3.3. UV Luminosity Function

The luminosity function (LF) is the density of galaxies per luminosity interval as a function of luminosity. The UV luminosity function can be used to trace the

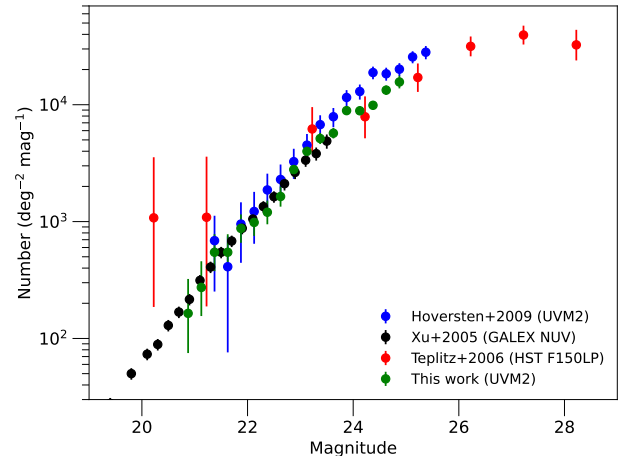


Figure 4. The UVM2 number counts (green) compared to GALEX NUV counts from Xu et al. (2005) (black), UVM2 number counts of CDF-S from Hoversten et al. (2009) (blue), and HST FUV number counts from Teplitz et al. (2006) (red). We see good agreement and differences can be attributed to survey area and exposure times. The corrections for MW extinction are minimal (~ 0.1 mag) as is the color difference between UVM2 and GALEX NUV. The correction to compare UVM2 and the HST values depends on the assumed spectrum of the observed source. A correction of -0.274 mag, based on a power law spectrum with slope -0.754 , is applied to the HST values.

evolution of the star formation rate density (SFRD) as the UV luminosity is a direct probe of recent star formation (Madau & Dickinson 2014). However, the SFRD as determined by UV luminosity is subject to high uncertainty due to the scaling relation from luminosity to star formation rate and the correction for dust attenuation. Often the IR is used in tandem, as composite SFR indicators are more precise and do not suffer from dust attenuation (Kennicutt & Evans 2012).

Here, we provide our measurements of the UV LF in the redshift range $0.2 < z < 1.2$ to build on previous work done by GALEX (Arnouts et al. 2005) and more recent works by Swift/UVOT (Hagen et al. 2015), XMM-Newton OM (Page et al. 2021; Sharma et al. 2022a,b), Astrosat UVIT (Bhattacharya et al. 2023), and HST (Sun et al. 2023).

First, we convert the observed UVM2 apparent magnitude of a source to an absolute magnitude using the measured redshift and the estimated K-correction from the code `kcorrect` (Blanton & Roweis 2007, version 5.0.1b). The K-correction is determined for each galaxy using the observed SED. For each observed object, we utilize the UVOT photometry; the Yang et al. (2014) photometry calculated using ground based UBVR_i, z' , and HK imaging from Capak et al. (2004), JH band

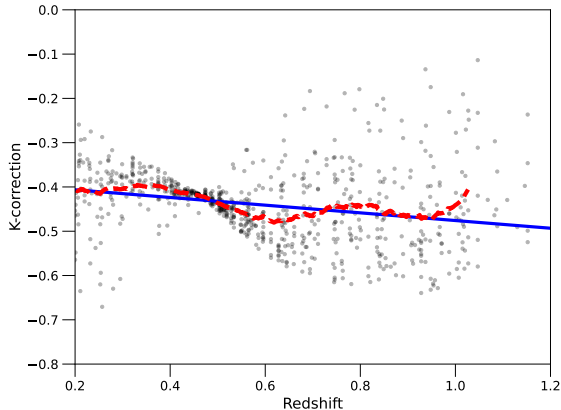


Figure 5. The K-correction as a function of redshift for galaxies above the 50% completeness threshold. We see that the K-correction shows a slight redshift dependence with scatter. We fit a linear function (blue line), which is a good fit to the running average (red dashed line). This regression is used in the calculation of the UV LF.

imaging from Keenan et al. (2010), Ks band imaging from Wang et al. (2010), and Spitzer IRAC data from Ashby et al. (2013); and the redshift value from Yang et al. (2014), of which over half are spectroscopic.

The absolute magnitude and redshift values are the data used to calculate the UV LF. We fit the UV LF using two methods, the traditional V_{\max} method and a more flexible Maximum Likelihood Estimation (MLE) approach. We will discuss how the LF is calculated for each method, their strengths and weaknesses, and the results from both approaches.

We utilize the Schechter (1976) functional form when fitting the LF:

$$\phi(M)dM = 0.4 \log(10) \phi^* \left(10^{0.4(M^*-M)}\right)^{\alpha+1} \times \exp(-10^{0.4(M^*-M)}) dM, \quad (2)$$

where $\phi(M)$ is the number density of galaxies of magnitude M , ϕ^* is the normalization, M^* is the characteristic magnitude at the exponential cutoff, and α is the faint-end slope.

To minimize uncertainty due to incompleteness, only galaxies above the 50% completeness limit are used when fitting the UV LF. Figure 5 shows the calculated K-correction as a function of redshift for galaxies above the 50% completeness limit. We see that the K-correction is only a weak function with redshift but with some scatter. In the construction of our UV LF, we assume a weak linear function with redshift to describe the K-correction.

After our completeness cut, we calculate the LF using 795 objects.

3.3.1. V_{\max} Method

Our first approach at fitting the UV LF is using the V_{\max} method introduced in Schmidt (1968). As this is a flux-limited survey, our completeness affects our ability to detect faint sources at high redshift. To account for this, the V_{\max} method relies on calculating the maximum volume in which a source could be observed multiplied by the completeness for that source magnitude. That is:

$$\phi(M)dM = \sum_i \frac{1}{C_i V_{\max,i}} \quad (3)$$

where C is the completeness fraction as calculated from the Fleming et al. (1995) function, and V_{\max} is the maximum volume in which the object could be detected by our survey. The LF is calculated with binned data to get discrete estimates of $\phi(M)$ by summing over the i in the magnitude bin. As the FUV absolute magnitudes are calculated using the observed UVM2 apparent magnitude, we utilize the UVM2 completeness curve. We also perform bootstrap resampling, similar to Hagen et al. (2015), to calculate errors on the discrete LF points. These discrete points are then fit with a Schechter function using a Levenberg–Marquardt least squares algorithm.

3.3.2. MLE

One downside of the V_{\max} method is the use of binned data. By changing the binning, the best fit parameters can vary. A MLE approach is more general and takes full advantage of the unbinned data and can be modified to incorporate photometric uncertainties (Page et al. 2021). Here, we use the likelihood function outlined in Ciardullo et al. (2013) but note that other likelihood functions are used in the literature (Page et al. 2021). One advantage of the likelihood function from Ciardullo et al. (2013) is the ability to jointly fit all three Schechter parameters compared to other approaches where the normalization is determined by the number of observed sources.

We briefly outline the likelihood function used here. For an observed luminosity function $\phi(L)\Delta L$, we can say the expected number of galaxies in the bin L to $L + \Delta L$ is $\lambda = \phi(L)\Delta L\Delta V$, where ΔV is the volume observed. As galaxies are being counted, the probability that you observe n galaxies is given by the Poisson distribution,

$$p(n) = \frac{\lambda^n e^{-\lambda}}{n!}.$$

Extended to the whole sample, the probability of seeing n_i galaxies in the bin L_i to $L_i + \Delta L$ is

$$P = \prod_i p(n_i) = \prod_i \frac{\lambda_i^{n_i} \exp(-\lambda_i)}{n_i!}.$$

In the limit where ΔV and ΔL go to dL and dV , we can say that in each bin, there is either 0 or 1 galaxy.

$$\begin{aligned} P &= \prod_{\text{bins with 0}} \exp(-\lambda_i) \prod_{\text{bins with 1}} \lambda_i \exp(-\lambda_i) \\ &= \prod_{\text{all bins}} \exp(-\lambda_i) \prod_{i=1}^N \lambda_i \\ &= \exp\left(-\sum_{\text{all bins}} \phi(L_i) dL dV\right) \prod_i^N \phi(L_i) dL dV, \end{aligned}$$

where N is the total number of sources.

The sum in the above equation can be re-written as an integral. When taking the log of the likelihood and dropping constant terms, we are left with

$$\ln P = -\int_{z_1}^{z_2} \int_{L_{\min}(z)}^{\infty} \phi(L) dL \frac{dV}{dz} dz + \sum_i^N \ln(\phi(L_i)), \quad (4)$$

where $L_{\min}(z)$ is the minimum luminosity that our sample is sensitive to. It is the luminosity corresponding to the 50% completeness limit at a given redshift, using the K-correction as a function of redshift described above.

We use the above likelihood function to estimate parameters that best fit the observed luminosity function. In order to understand covariances in the data and get error estimates, we perform Markov Chain Monte Carlo (MCMC) sampling using `emcee` (Foreman-Mackey et al. 2013). We first determine the parameters that minimize $-\ln P$ using standard minimization techniques. This initial estimate is used as the starting point for the walkers. By starting the walkers in the region of highest likelihood, we reduce the burn-in time. The posterior distributions we get from the MCMC sampling give us median values for the parameters as well as errors on the estimated value. An example of our 2D posteriors when determining the UV LF for the entire sample are shown in Figure 6.

To get information regarding evolution with redshift, we subdivide our sample into four redshift bins and calculate the LF in each. The redshift bins are $0.2 < z < 0.4$, $0.4 < z < 0.6$, $0.6 < z < 0.8$, and $0.8 < z < 1.2$. Our best fit Schechter parameters and errors are given in Table 3.

For the full sample, both the MLE and V_{\max} results are given. In each redshift bin, we provide the MLE

values. Previous UV LF work using UVOT (Hagen et al. 2015) was unable to constrain α in any redshift bin. Here, we are able to estimate α in the two lowest redshift bins and give the results with α as a free parameter. We also report the MLE values when we fix α using the values determined in Arnouts et al. (2005). We note that other results from this redshift range (e.g. Oesch et al. 2010; Moutard et al. 2020; Page et al. 2021; Sharma et al. 2022b) find α estimates with a large dispersion, making it difficult to determine any evolution in α over this redshift range. Recent work by Bhattacharya et al. (2023) finds evolution in α using UVIT.

The UV LF as determined using MLE is shown in Figure 7 for each redshift bins, with the discrete V_{\max} points as a reference. We note that there is a slight turn down in the faintest bins. Specifically in the lowest redshift bin, this is likely related to the extended source discussion in § 3.1, where we may be overestimating the completeness in the faintest magnitude bins. Additionally, the lowest absolute magnitude bins only contain a few objects. As a result, the bootstrap error is an underestimate. The shaded region is determined using the one σ errors for M^* and ϕ^* .

3.4. SFRD

With Schechter function fits in various redshift bins, the star formation rate density as a function of redshift is calculated. First, the Schechter function must be integrated to get the luminosity density. In terms of the Schechter parameters, the luminosity density is given by:

$$\rho_{\text{UV}} = \int_0^{\infty} L \phi(L) dL = \phi^* L^* \Gamma(2 + \alpha),$$

where Γ is the gamma function. As α becomes steeper, small changes in α can greatly affect the luminosity density. For the extremes in α here, the ratio of $\Gamma(2 - 1.6)/\Gamma(2 - 1.19)$ is roughly 2. A non-zero lower limit on the integral changes the gamma function to the incomplete gamma function. A lower limit of $0.03 L^*$ is frequently assumed and is adopted here.

This luminosity density can then be corrected for the effects of dust and converted into a star formation rate density. However, several simplifying assumptions must be made. First, the shape of the dust attenuation law is known to vary between different galaxies (Salim et al. 2018), within a single galaxy (Declair et al. 2019), and as a function of redshift (Bogdanoska & Burgarella 2020; Markov et al. 2024). A common approach to estimate

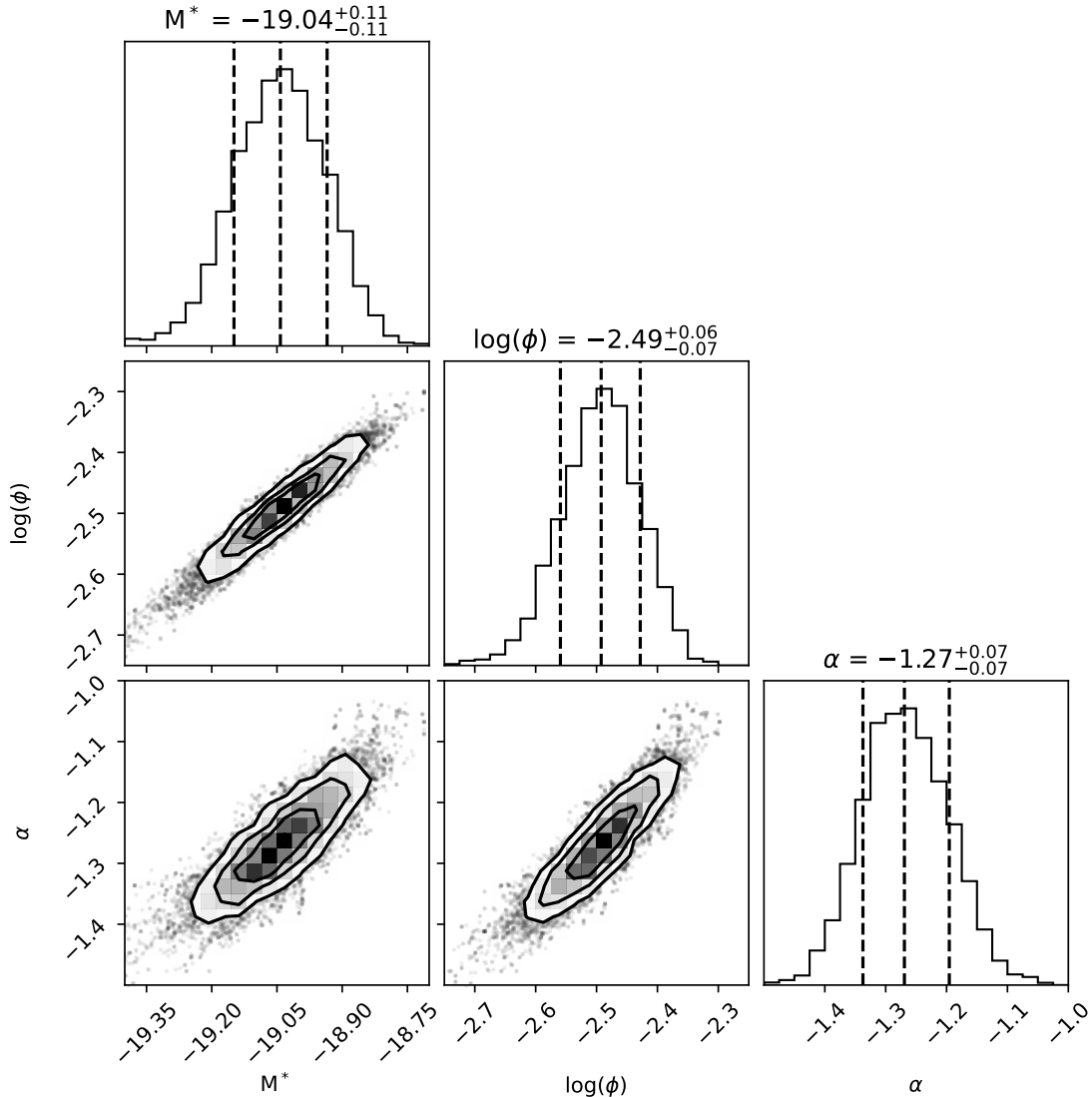


Figure 6. The diagnostic corner plot shows the Schechter function parameter estimates for the entire sample of galaxies across the whole redshift range. This diagnostic plot shows the covariances between the different parameters. However, the one dimensional posteriors are well fit with a Gaussian.

the amount of attenuation is to use IRX- β relationship from Meurer et al. (1999), where β is the UV spectral slope $F_\lambda \propto \lambda^\beta$. However, recent works have found evidence that there is significant scatter in the IRX- β relationship due to variations in the underlying dust attenuation curves (Salim & Boquien 2019). Work in dust attenuation have probed whether the observed attenuation is correlated with galaxy properties like optical opacity, metallicity, and inclination angle (Salim et al. 2018; Shivaei et al. 2020; Battisti et al. 2017).

Typically a $A_{FUV} - \beta$ is assumed to correct the luminosity density despite the uncertainty. Salim & Boquien (2019) proposed introducing additional terms to the $A_{FUV} - \beta$ relationship to reduce the impact of scatter,

specifically recommending using stellar mass or Balmer optical depth. However, stellar mass estimates require the use of another, possibly uncertain, scaling relation or spectral energy distribution fitting, while Balmer optical depth requires spectra. Additionally, there is uncertainty in how well the nebular attenuation, parameterized by the Balmer decrement, traces the UV continuum attenuation as line emission and stellar emission are distinct. The line emission is due to the most massive stars embedded in birth clouds, while the stellar UV emission comes from stars that are only attenuated by the ambient ISM (Charlot & Fall 2000; Salim et al. 2018).

The scaling relation to go from luminosity is more well understood but the exact calibration can vary. Within

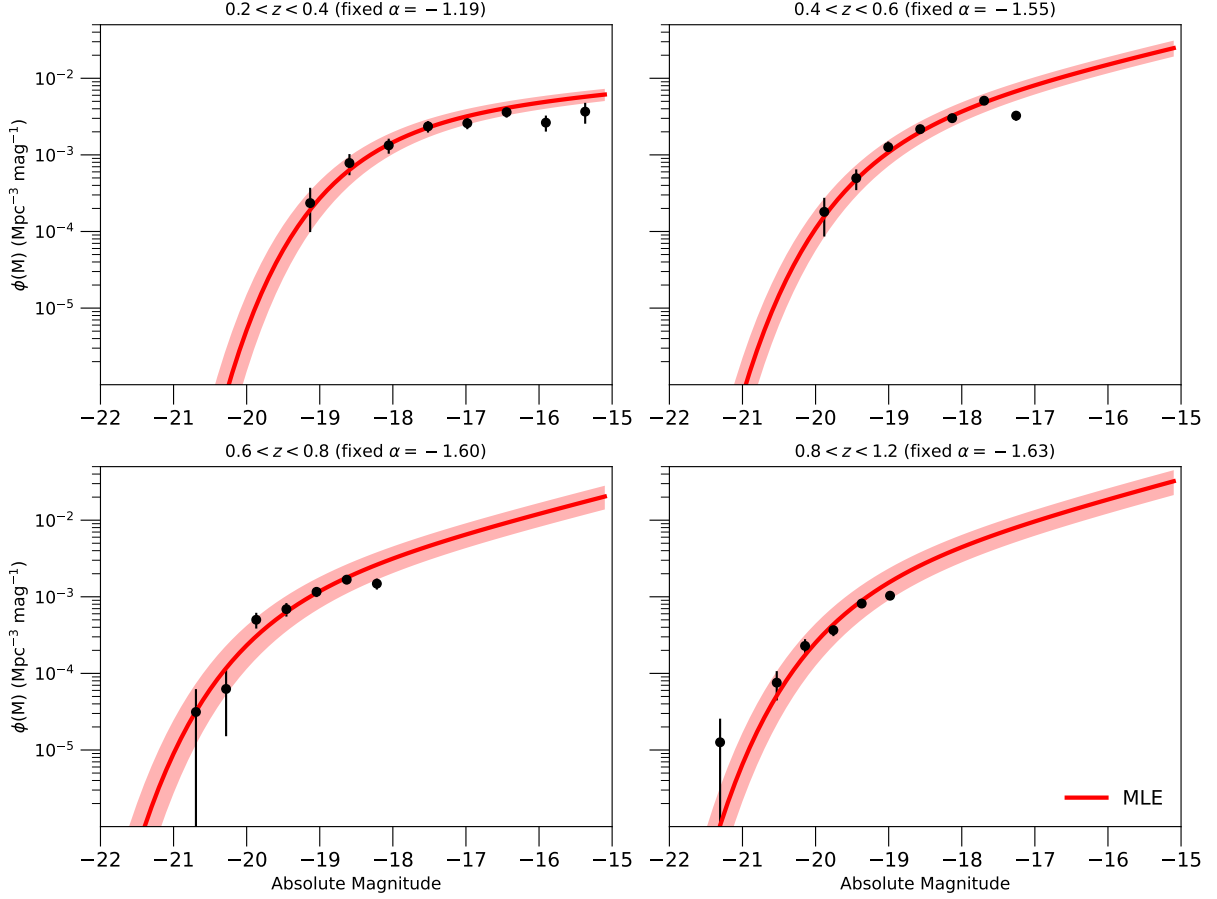


Figure 7. The UV LF in four different redshift bins as determined using UVOT observations of GOODS-N. The black dots are from the V_{\max} method with errors from bootstrap resampling. The faintest bins are only comprised of a handful of galaxies due to incompleteness. As a result, the bootstrap error estimates are likely an underestimate of the true error. The solid red line is the MLE best fit Schechter function with the shaded region showing the 1σ uncertainty from M^* and ϕ^* . In each redshift bin, α is fixed using the values from [Arnouts et al. \(2005\)](#). We see clear evolution in M^* . The best fit LF is integrated to calculate the UV luminosity density which is converted to a star formation rate density using the scaling relation from [Kennicutt \(1998\)](#).

Table 3. Best fit Schechter function parameters

Redshift range	M^*	$\phi^*/10^{-3}$	α ^a	SFRD _{uncorr} /10 ⁻²
	(Mag)	(Mpc ⁻³)		(M_{\odot} yr ⁻¹ Mpc ⁻³)
Full sample (V_{\max})	-19.05 ± 0.11	2.90 ± 0.41	-1.086 ± 0.074	—
Full sample (MLE)	-19.04 ± 0.11	3.21 ± 0.48	-1.267 ± 0.071	—
0.2-0.4 (free α)	-18.25 ± 0.41	3.34 ± 1.47	-1.31 ± 0.20	—
0.4-0.6 (free α)	-18.66 ± 0.29	5.59 ± 2.21	-1.40 ± 0.23	—
0.2-0.4 (fixed α)	-18.00 ± 0.17	4.29 ± 0.61	-1.19	$0.65^{+0.22}_{-0.17}$
0.4-0.6 (fixed α)	-18.81 ± 0.14	4.23 ± 0.69	-1.55	$1.94^{+0.62}_{-0.51}$
0.6-0.8 (fixed α)	-19.37 ± 0.18	2.13 ± 0.59	-1.6	$1.77^{+0.83}_{-0.64}$
0.8-1.2 (fixed α)	-19.23 ± 0.14	3.26 ± 0.92	-1.63	$2.53^{+1.16}_{-0.94}$

^aFixed values for α are taken from [Arnouts et al. \(2005\)](#).

the scaling relation used are assumptions about the initial mass function (IMF) and star formation history (SFH). Whether or not the IMF is universal is the cause of some debate (Bastian et al. 2010). The SFH is expected to vary from galaxy to galaxy based on several stochastic factors such as merger rates, available gas mass, and star formation efficiency.

With these caveats, we use the relation from Meurer et al. (1999),

$$A_{FUV} = 4.43 + 1.99\beta,$$

where β is the observed UV slope calculated between 1250 and 2600 Å, to correct for dust. This slope is historically measured using spectra. However, β measured from photometric colors became common due to the ubiquity of GALEX data (Kong et al. 2004). We estimate β from a power law fit to photometry corresponding to a rest frame wavelength between 1250 and 2800 Å. In addition to the canonical relation from Meurer et al. (1999), we also explore the $A_{FUV} - \beta$ relationship from Overzier et al. (2011) which uses the same sample and improved aperture matching and finds less attenuation for a fixed β . Other empirically measured IRX- β relationships are given in Takeuchi et al. (2012) and Casey et al. (2014).

We use the SFR scaling relation from Kennicutt (1998),

$$\text{SFR}(\text{UV}) = 1.4 \times 10^{-28} L_{\text{UV}}.$$

The updated SFR indicator from Kennicutt & Evans (2012), based on Hao et al. (2011) and Murphy et al. (2011), will be discussed later.

As the attenuation correction is highly uncertain, the uncorrected (observed) SFRD is typically reported and is given in Table 3 for each redshift bin. We will discuss how these chosen scaling relations affect the interpretation of the results in Section 4.3.

3.5. Redshift Evolution

With our sample binned by redshift, we are able to explore redshift evolution of the galaxy population over a large fraction of the age of the Universe.

Figure 8 shows the luminosity density in the four different redshift bins as well as lines showing different rates of evolution. We fit a power law and find that the observed luminosity density evolves as $(1+z)^{3.04 \pm 1.38}$ with the observed luminosity density $\log(\rho) = 25.44 \pm 0.27$ at $z \sim 0$. This redshift evolution is consistent with the evolution reported in Schiminovich et al. (2005) and Hagen et al. (2015). Wyder et al. (2005) calculated the observed luminosity density and found a value of

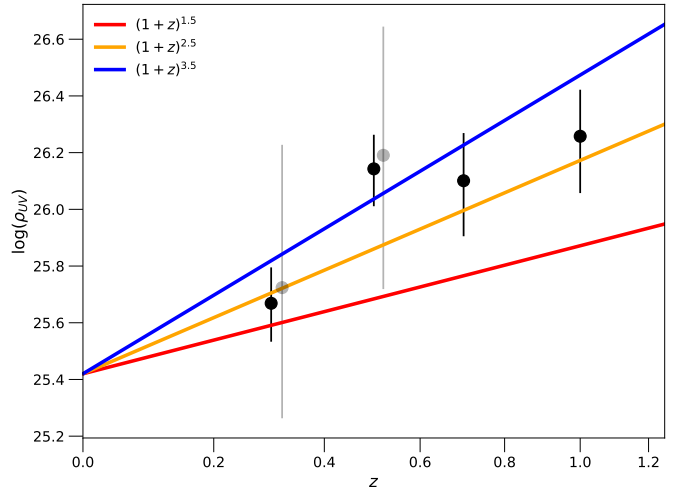


Figure 8. The observed UV luminosity density $\log(\rho_{\text{UV}})$ as a function of redshift. The grey points are from the MLE fits with α as a free parameter, while the black points are with α fixed using the values in Arnouts et al. (2005). We fit a power law evolution model of the form $\log(\rho_{\text{UV}}) \propto (1+z)^n$. The best fit model is $n = 3.04 \pm 1.38$. Using the intercept from the fit, we plot different evolution models corresponding to $n = 1.5$ (red), 2.5 (yellow), 3.5 (blue).

$\log(\rho_{\text{UV}}) = 25.55 \pm 0.12$, consistent with our results. This Figure also shows how our values for the UV luminosity density are consistent between our fits whether α is fixed (solid black) or free (grey). However, due to the degeneracies between the LF parameters, the errors are much larger when α is left as a free parameter.

4. DISCUSSION

4.1. Comparison to Literature

4.1.1. Number Counts

As in Hoversten et al. (2009), we have shown the utility of using repeat UVOT observations of the same field to get deep photometry of star-forming galaxies at $z < 1.5$. Our number counts agree with past literature results from GALEX NUV (Xu et al. 2005) and Swift/UVOT (Hoversten et al. 2009) and are qualitatively similar to the FUV number counts from HST (Teplitz et al. 2006).

UVOT occupies a unique niche between GALEX and HST. While UVOT does not go as deep as HST or as wide as GALEX, it can achieve depths of $m_{AB} \sim 24$ in short observations of a few kiloseconds per day taken over the course of a year in a larger area than could be observed by HST in a single pointing. This approach has the advantage of ease of scheduling as the short daily observations are spread over a long time frame, less susceptibility to cosmic variance, and moderate depth possible to get scarce UV data of galaxies at $z \lesssim 1.5$.

4.1.2. Luminosity Function

We calculate the best fit LF of our entire sample as well as in four distinct redshift bins. Our best fit LF in each redshift bin shows evolution in M^* consistent with other works. Hagen et al. (2015), which also used UVOT data to determine the UV LF in CDF-S, could not constrain the faint end slope α . Here, we are able to constrain α but only for the two lowest redshift bins. For ease of comparison, we fix α using the values from Arnouts et al. (2005) like in Hagen et al. (2015). Measurements of α show large scatter around $\alpha \sim -1.5$ between $0.5 < z < 2$ (Oesch et al. 2010; Alavi et al. 2016) making it difficult to quantify its evolution.

From our best fit UV LF, we find less luminous characteristic magnitudes compared to Hagen et al. (2015). The very luminous values in Hagen et al. (2015) was noted by Sharma et al. (2022a). They posited that the discrepancy could be the result of how galaxies were selected. Hagen et al. (2015) used the SExtractor parameters from Hoversten et al. (2009) to create their sample, specifically detecting sources with the u band image. Here, we use SExtractor in a two phase approach and utilize a meta-image for detections made from the summed UVW2, UVM2, and UVW1 images. We specifically exclude the u band to minimize the effects of the higher background. However, by excluding the u band, we may be missing red sources or those in the highest redshift bin not detected by the blue filters.

The quoted 50% completeness level in Hagen et al. (2015) is $m_{AB} = 24.1$ for u band in roughly 125 ks. Here, using a different detection methodology we find 50% completeness down to 23.85 mag in only 73 ks. The differences in M^* is unlikely to be due to cosmic variance as Sharma et al. (2022a) using XMM-Newton OM data of the CDF-S field found less luminous characteristic magnitudes that agree with our results here.

The differences in our detection method compared to Hagen et al. (2015) could also explain our ability to determine the faint end slope in the two lowest redshift bins. While the previous work by Hagen et al. (2015) had deeper data than what is presented here, with our different source selection methodology, we are able to achieve similar depths and constrain α in the two lowest redshift bins.

Additionally, Page et al. (2021) raised the issue of AGN contamination skewing the UV LF. Here, we do not see a measurable difference in M^* when including X-ray detected sources. However, we agree that the non-thermal emission from AGN can significantly affect the UV LF and bias conclusions made about the star-forming galaxy population and therefore, we have excluded them.

When looking at the UV luminosity density, we find the expected evolution over the redshift range as shown in Figure 8. Schiminovich et al. (2005) using GALEX data finds the UV luminosity density evolves as $(1+z)^{2.5 \pm 0.7}$ at $z < 1$; for $z > 1$, they find the power law index to be (0.5 ± 0.4) . This is compared to our evolution which goes as $(1+z)^{\sim 3}$. Schiminovich et al. (2005) has a similar number of galaxies to our work but over a larger area due to the source confusion limitation of GALEX. Our evolution is also faster than the values found by Hagen et al. (2015) but do agree within the 1σ errors (1.88 ± 1.32).

Schiminovich et al. (2005) explored the UV luminosity density evolution of a subset of UV luminous galaxies ($M < -19.32$), finding more rapid evolution, $(1+z)^5$. Our sample contains only a few of these very UV luminous galaxies so a direct comparison is difficult. For the two higher redshift bins, the luminosity density values found here agree with the values reported in Sharma et al. (2022b).

We compare the observed luminosity density found here with recent results in the literature and early results from GALEX. Figure 9 shows the observed luminosity density from a variety of studies compared to the results here. We see relatively good agreement across the entire redshift range. However, scatter is present as each studies observes a different area and location on the sky. A larger analysis combining these results could provide tighter constraints on the global UV luminosity density evolution over this redshift range.

We also test how the redshift bins affect the derived evolution. To do so, we use finer redshift bins (width of 0.1 from $z = 0.2$ to $z = 0.7$, 0.2 from $z = 0.7 - 0.9$, and 0.3 between $z = 0.9 - 1.2$). We again fix α using the values from Arnouts et al. (2005). We find that the uncorrected UV luminosity density evolves with a power law index of 3.21 ± 0.96 with this binning scheme, agreeing with the evolution determined above.

4.2. UV SF Scaling Relations

Understanding the redshift evolution of the UV LF is of great interest as it is a direct tracer of star formation over cosmic time. However, in addition to systematics like cosmic variance, it is not necessarily straightforward to correct for the effects of dust attenuation and to convert from a UV luminosity to a SFR.

The scaling relation we used for calculating SFR in Section 3 is the canonical result from Kennicutt (1998). However, more recent calibrations exist from Hao et al. (2011) and Murphy et al. (2011). Additionally, McQuinn et al. (2015) provides a SFR calibration using local volume dwarf galaxies. The K98 scaling relation is

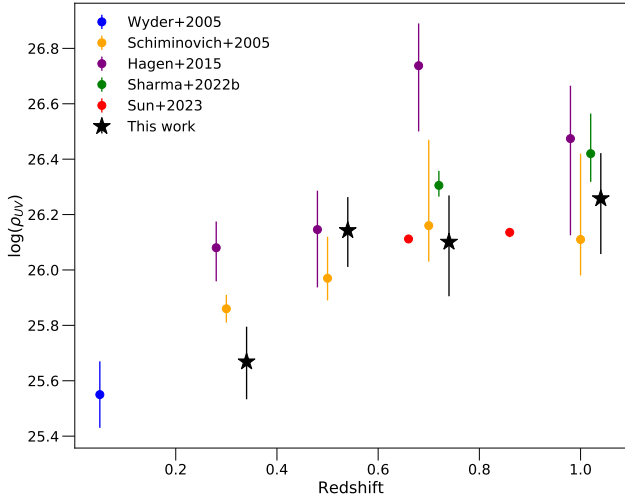


Figure 9. Our observed luminosity density (black stars) as a function of redshift compared to Wyder et al. (2005) (blue), Schiminovich et al. (2005) (yellow), Hagen et al. (2015) (purple), Sharma et al. (2022b) (green), and Sun et al. (2023) (red). We see good agreement across all redshift bins. We focus on observed UV luminosity density as the chosen dust attenuation correction and SFR calibrations differ.

intermediate between the more recent results. Specifically, Hao et al. (2011) gives SFRs that are 68% of those from K98 and the McQuinn et al. (2015) values are $1.46\times$ larger than K98. This factor of two discrepancy between the extremes is a severe limitation in determining the normalization for the changing SFRD with redshift.

To better constrain SFR, composite SFR indicators are commonly used as monochromatic SFR indicators are much less reliable. By combining the UV and total IR emission or possibly emission line diagnostics, the SFR can be determined more precisely (Calzetti 2013; Kennicutt & Evans 2012; Madau & Dickinson 2014). However, practically this can be an issue as observations at UV and IR wavelengths require observations from different facilities. These multiwavelength observations may not exist for the field of interest.

Leja et al. (2019) showed that SED fitting of 5000+ galaxies at $0.5 < z < 2.5$ produced SFRs that were 0.1 to 1 dex lower than the standard UV+IR indicators. They explain the discrepancy as due to the emission of stars older than 100 Myr. Performing SED fitting on this sample of galaxies would be an interesting test of the accuracy of the standard SFR scaling relations.

4.3. Impact of Assumed Dust Attenuation Correction

In addition to the uncertainty in the normalization of the SFRD caused by the SFR indicator chosen, correcting for the effects of internal dust attenuation can af-

fect the normalization and evolution of the SFRD. The effects of dust attenuation are highly uncertain; a variety of dust attenuation curves have been observed in galaxies, with the biggest discrepancies and highest uncertainties in the UV. The empirical IRX- β relationship as defined in Meurer et al. (1999) is typically used to estimate the attenuation in the FUV band from the observed UV spectral slope.

At its simplest, the attenuation law has been seen to vary between a shallow curve such as the starburst law reported in Calzetti et al. (2000) and the SMC extinction law. At 1500 Å, these curves vary drastically. In terms of A_V , the attenuation at 5500 Å, the FUV attenuation from the SMC curve is $4.77A_V$ compared to $2.55A_V$ for the Calzetti law. For a dusty galaxy with $A_V = 1$, these corrections differ by more than 2 mag, almost an order of magnitude difference in luminosity.

To correct our sample here for dust, we use the median UV slope β to calculate A_{FUV} for each redshift bin. β was originally defined as a fit to 10 wavelength windows from UV spectra (Calzetti et al. 1994). Robustly calculating it from photometry alone is challenging. Often, at low redshift, β is estimated using the GALEX FUV-NUV color (Kong et al. 2004). While the Calzetti et al. (1994) windows range from 1250-2600 Å, some works use photometry out to 3000 Å which can affect the fit. The different methodologies used to calculate β can complicate comparing across studies.

For each galaxy, a power law was fit to photometry corresponding to a rest frame wavelength between 1250 and 2600 Å in order to estimate β . For every redshift bin, we find the median β to be roughly -1.2 but with significant scatter, where β ranges from -2.5 to $+1$. Bogdanoska & Burgarella (2020) predicts that the FUV attenuation, which is often estimated using β , should increase rapidly up to $z \sim 2$. Kurczynski et al. (2014) using HST data calculated β for galaxies across the redshift range $1 < z < 8$, finding that the highest redshift galaxies were bluer and that the redshift evolution was strongest in the faintest galaxies.

Figure 10 shows β versus absolute UV magnitude and redshift for this sample. Also shown are the median value and 1σ error in each bin and the evolution in β with respect to M_{UV} or z reported in Kurczynski et al. (2014), extrapolated from $z \sim 1$. In terms of β and by extension, A_{FUV} , we see no obvious evolution with redshift, contrary to some predictions in the literature. We also see no noticeable trend with absolute magnitude. Due to the large scatter in β , our values are not in tension with β evolving as a function of M_{UV} and z . It is also possible that due to our selection methodology, we are missing many highly attenuated sources. Regardless,

it is clear that the large scatter in β is more significant than any evolution with redshift or magnitude.

The median A_{FUV} in each redshift bin was determined using the Meurer et al. (1999) relationship. However, the reanalysis of the original starburst sample by Overzier et al. (2011) finds the attenuation is roughly 0.5 mag less after the improved aperture matching. Because of these differences, the IRX- β calibration assumed is another uncertainty that can greatly affect the normalization of the dust-corrected SFRD.

Using the FUV attenuation corresponding to the median β in each redshift bin, we find the corrected luminosity density scales as $(1+z)^{2.97 \pm 1.10}$ with $\log(\rho) = 26.28 \pm 0.22$ at $z = 0$. This evolution is in line with the UV+IR evolution from Madau & Dickinson (2014). If we found that attenuation at $z \sim 1$ was greater, the evolution in the dust-corrected SFRD would be much faster than the consensus value.

We investigate β as a function of redshift or absolute magnitude by looking at studies of higher redshifts. Bouwens et al. (2009) find that more luminous galaxies are more attenuated and therefore have redder UV slopes for a sample of UV selected galaxies at $z \sim 2.5$. Meanwhile, Reddy et al. (2008, 2018) found no correlation between the dust attenuation and observed UV luminosity at $z \sim 2$. Finkelstein et al. (2012) and Bouwens et al. (2014) find evidence of a correlation at $z \sim 6$ and $z \sim 4$, respectively.

Looking at other works at these low redshifts, Mondal et al. (2023a) found no correlation between UV magnitude and β at $0.4 < z < 0.75$ using Astrosat UVIT. A similar study by Sharma et al. (2024) investigated the dust properties of XMM-Newton OM UVW1 selected galaxies in CDF-S using a stacking analysis of Herschel PACS and SPIRE data. They find that IRX, a proxy for attenuation, is highest at low UV luminosities for galaxies at $z = 0.6 - 1.2$. Prior GALEX work by Xu et al. (2007) found that for $z \sim 0.6$ UV selected galaxies, IRX does not vary with L_{UV} but that $z \sim 0$ galaxies show a dependence where IRX is less at low UV luminosities. For our sample of UV selected galaxies at $z < 1.2$, we find no correlation between β and absolute UV magnitude.

There is a lack of consensus, especially at low redshift, as to whether UV luminosity and attenuation are correlated. Selection effects are also a concern. As this sample is selected solely using the three near-UV filters of UVOT, highly obscured sources may be missed. These sources would have both low observed luminosities and red UV slopes. Additionally, the low redshift bins probe a relatively small volume, so cosmic variance could explain the paucity of red, luminous sources.

As mentioned, some studies such as Finkelstein et al. (2012) and Bouwens et al. (2014) see a $\beta - L_{UV}$ relationship at high redshift, where low luminosity galaxies are bluer. As strong evidence for a relationship is not seen in studies of the low redshifts, the lack of a trend at low z could be due to changes over cosmic time, specifically evolution in the interactions between the massive UV-emitting stars and the ISM. For young galaxies, dust is highly concentrated in star-forming regions, where the UV attenuation will be strongest. Later, through multiple generations of star formation, stellar feedback mixes the ISM, causing the dust to become diffuse across the entire galaxy rather than located near the site of star formation. Along with this different star-dust geometry at low redshift, age and metallicity differences become more apparent, and in turn will affect the color of galaxies. Any trend between UV emission from massive star formation and dust attenuation may be obscured as the star-dust geometry becomes more complex and age and metallicity become important factors.

This is seen in Narayanan et al. (2018a), which investigated the physical cause of dust attenuation law variations using cosmological simulations. They assume a single underlying extinction law and model the effects that geometry and radiative transfer have on the net attenuation law over cosmological time. They find that at $z \sim 6$, the attenuation law shows only small variations due to galaxies at this redshift having relatively uniform stellar ages and less dispersion in the star-dust geometry. However as galaxies evolve, the dispersion in attenuation curve shapes at $z \sim 0$ becomes substantial.

For this sample of UV selected galaxies at $0.2 \leq z \leq 1.2$, β is relatively constant with respect to both redshift and absolute magnitude. This shows that, specifically at lower redshifts, dust attenuation is not a simple function of redshift or luminosity. The scatter is driven primarily by differences between galaxies. The lack of obvious redshift evolution in β and consequently FUV attenuation is likely due to the great variation in dust attenuation between galaxies at low redshift.

Another complication is the various different empirical IRX- β relationships reported in the literature. For starburst galaxies, there is little scatter relative to the Meurer et al. (1999) curve. However, for normal star-forming galaxies, there is significant scatter. Narayanan et al. (2018b) explores the origin of the scatter seen in the IRX- β relationship. They show that the age of the stellar population, the geometry of the stars and dust, and the underlying extinction law can all shift the IRX- β relation away from the standard curve from Meurer et al. (1999). By detailed modeling of the stellar populations via SED fitting, the attenuation curve can be estimated.

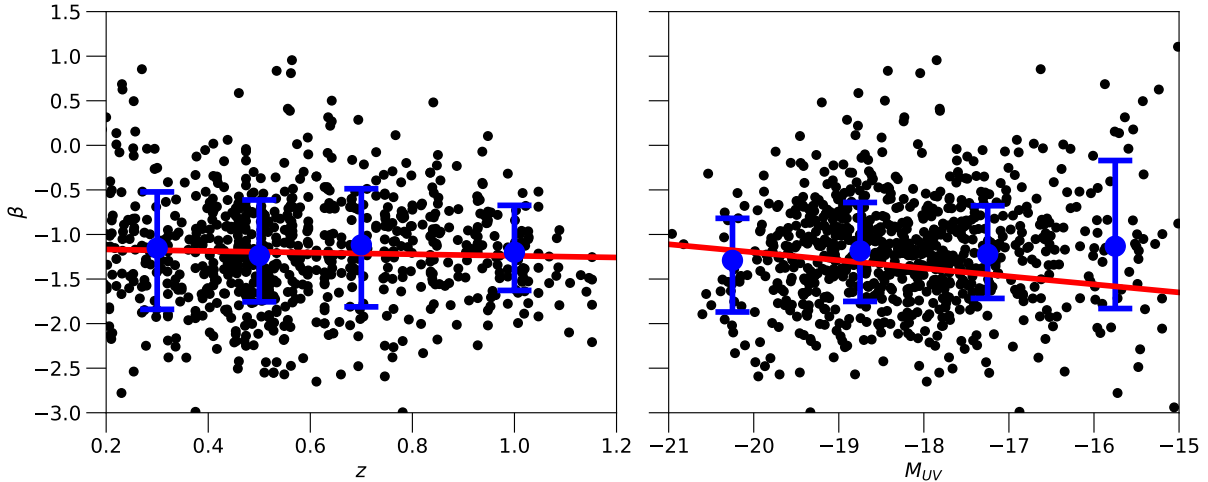


Figure 10. The UV spectral slope β as a function of absolute UV magnitude and redshift. We plot the measured UV slopes of each galaxy used in calculating the LF (black points), the median value in a given bin (blue points), and the 16th and 84th percentiles (blue errorbars). The red line shows the change in β with respect to M_{UV} and z found in Kurczynski et al. (2014), extrapolated the $z \sim 1$ down to $z \sim 0$. Here, we find no strong trend at $z < 1$ but the observed relationship from Kurczynski et al. (2014) is not ruled out due to the large scatter in β . We investigate further by investigating the redshift trend (left) in smaller magnitude bins and find no trend. Similarly, we bin the magnitude relation (right) in smaller time bins and again find no trend.

Otherwise, there will be uncertainty in the efficacy of using the standard Meurer et al. (1999) correction, as it corresponds to a Calzetti et al. (2000) attenuation law.

Ideally, as we have UV slope information for each galaxy in our sample, we could calculate the UV LF using the dust corrected luminosities. This would be preferable as the individual galaxies that comprise the sample can have varying attenuation curves. In terms of the Schechter parameters, correcting for dust prior to fitting the UV LF would have the largest effect on L^* but could also have a small effect on the faint end slope α as galaxies observed as UV faint could simply be highly obscured. For a fixed L^* and ϕ^* , a flattening of the faint end slope would lead to a smaller luminosity density and SFRD. However, in practice it is challenging to accurately account for things like completeness in calculating the UV LF after correcting individual galaxies for dust.

5. CONCLUSIONS

In this work, we present deep ultraviolet observations of the GOODS-North field using the UVOT aboard the Neil Gehrels Swift Observatory. These data complement previous UVOT observations of CDF-S as well as the extensive multiwavelength observations of GOODS-N in the literature. We catalog all detected sources, provide color information from the four filters spanning the near UV, and cross-match our objects with Yang et al. (2014) to construct SEDs ranging from the UV to IR.

We report a catalog of 1000+ sources identified in at least one of four UV bands. The UV galaxy number counts as a function of apparent magnitude are calculated and in good agreement with previous results from GALEX, Swift/UVOT and HST. After cross-matching our catalog with Yang et al. (2014), we perform K-corrections to our UV data to get the absolute FUV magnitudes of the detected galaxies. Our main results are as follows:

1. Using both V_{\max} and MLE methods, we fit the LF with a Schechter function in four different redshift bins between $0.2 < z < 1.2$. We find evidence for evolution of M^* , consistent with other works. Compared to prior UVOT observations of CDF-S, we find fainter characteristic luminosities and are able to constrain the faint-end slope α in the two lowest redshift bins. For ease of comparison with the literature, we fix α using the GALEX results from Arnouts et al. (2005).
2. Using our best fit LFs, we calculate the luminosity density and star formation rate density evolution. Using the color information provided by UVOT, we calculate β from the observed photometry and use the IRX- β relation from Meurer et al. (1999) to correct for the effect of dust attenuation. Our dust corrected SFRD agrees with previous results.
3. We discuss that different star formation rate scaling relations can change the SFRD normalization

by a factor of two. Additionally, we discuss the difficulty in correcting for dust attenuation, which can have a large impact on the evolution and normalization of the corrected SFRD. In particular, we highlight the large observed spread in β seen for galaxies in this redshift range.

4. Compared to studies at high redshift, we do not find strong evidence that β is correlated with UV luminosity or redshift. As a redshift and UV luminosity dependence is seen in UV selected samples of high redshift galaxies and not surveys at $z \sim 1$ implies that galaxy to galaxy differences in dust attenuation at low redshift are stronger than any evolution in β with respect to L_{UV} or z , likely driven by the complex interplay between star formation and the ISM.

While the field pushes towards studying large samples of high redshift objects, understanding the UV emission of low to intermediate redshift galaxies is important to fully track the evolution in star formation over cosmic time. At these low redshifts, the differences between dust attenuation in these galaxies complicates studying the evolution in the star formation rate density. Using the sample of galaxies provided here, further work is possible by modeling the full spectral energy distributions in order to better constrain dust attenuation and compare SED fitting derived SFRs to the standard scaling relations.

ACKNOWLEDGEMENTS

The authors wish to thank the anonymous referee for comments that greatly improved this manuscript. We acknowledge sponsorship at the Pennsylvania State University by NASA contract NAS5-00136. This research was also supported by the NASA Astrophysics Data Analysis Program (ADAP) through grant NNX16AF35G. The Institute for Gravitation and the Cosmos is supported by the Eberly College of Science and the Office of the Senior Vice President for Research at the Pennsylvania State University. MJP acknowledges support from the UK Space Agency, grant number ST/X002055/1. We thank Gautam Nagaraj for conversations regarding processing UVOT deep field data. This research has made use of NASA's Astrophysics Data System. This research has made use of data and/or software provided by the High Energy Astrophysics Science Archive Research Center (HEASARC), which is a service of the Astrophysics Science Division at NASA/GSFC and the High Energy Astrophysics Division of the Smithsonian Astrophysical Observatory.

Software: Astropy (Astropy Collaboration et al. 2013, 2018, 2022), `kcorrect` (Blanton & Roweis 2007, version 5.0.1b), `emcee` (Foreman-Mackey et al. 2013), `corner` (Foreman-Mackey 2016).

REFERENCES

- Alavi, A., Siana, B., Richard, J., et al. 2016, ApJ, 832, 56, doi: [10.3847/0004-637X/832/1/56](https://doi.org/10.3847/0004-637X/832/1/56)
- Alexander, D. M., Bauer, F. E., Brandt, W. N., et al. 2003, AJ, 126, 539, doi: [10.1086/376473](https://doi.org/10.1086/376473)
- Antonucci, M., Talavera, A., Vagnetti, F., et al. 2015, A&A, 574, A49, doi: [10.1051/0004-6361/201425010](https://doi.org/10.1051/0004-6361/201425010)
- Arnouts, S., Schiminovich, D., Ilbert, O., et al. 2005, ApJL, 619, L43, doi: [10.1086/426733](https://doi.org/10.1086/426733)
- Ashby, M. L. N., Willner, S. P., Fazio, G. G., et al. 2013, ApJ, 769, 80, doi: [10.1088/0004-637X/769/1/80](https://doi.org/10.1088/0004-637X/769/1/80)
- Astropy Collaboration, Robitaille, T. P., Tollerud, E. J., et al. 2013, A&A, 558, A33, doi: [10.1051/0004-6361/201322068](https://doi.org/10.1051/0004-6361/201322068)
- Astropy Collaboration, Price-Whelan, A. M., Sipőcz, B. M., et al. 2018, AJ, 156, 123, doi: [10.3847/1538-3881/aabc4f](https://doi.org/10.3847/1538-3881/aabc4f)
- Astropy Collaboration, Price-Whelan, A. M., Lim, P. L., et al. 2022, apj, 935, 167, doi: [10.3847/1538-4357/ac7c74](https://doi.org/10.3847/1538-4357/ac7c74)
- Barro, G., Pérez-González, P. G., Cava, A., et al. 2019, ApJS, 243, 22, doi: [10.3847/1538-4365/ab23f2](https://doi.org/10.3847/1538-4365/ab23f2)
- Bastian, N., Covey, K. R., & Meyer, M. R. 2010, ARA&A, 48, 339, doi: [10.1146/annurev-astro-082708-101642](https://doi.org/10.1146/annurev-astro-082708-101642)
- Basu-Zych, A. R., Hornschemeier, A. E., Hoversten, E. A., Lehmer, B., & Gronwall, C. 2011, ApJ, 739, 98, doi: [10.1088/0004-637X/739/2/98](https://doi.org/10.1088/0004-637X/739/2/98)
- Battisti, A. J., Calzetti, D., & Chary, R. R. 2017, ApJ, 851, 90, doi: [10.3847/1538-4357/aa9a43](https://doi.org/10.3847/1538-4357/aa9a43)
- Bertin, E., & Arnouts, S. 1996, A&AS, 117, 393, doi: [10.1051/aas:1996164](https://doi.org/10.1051/aas:1996164)
- Bhattacharya, S., Saha, K., & Mondal, C. 2023, arXiv e-prints, arXiv:2310.01903, doi: [10.48550/arXiv.2310.01903](https://doi.org/10.48550/arXiv.2310.01903)
- Blanton, M. R., & Roweis, S. 2007, AJ, 133, 734, doi: [10.1086/510127](https://doi.org/10.1086/510127)
- Bogdanoska, J., & Burgarella, D. 2020, MNRAS, 496, 5341, doi: [10.1093/mnras/staa1928](https://doi.org/10.1093/mnras/staa1928)
- Bouwens, R. J., Illingworth, G. D., Franx, M., et al. 2009, ApJ, 705, 936, doi: [10.1088/0004-637X/705/1/936](https://doi.org/10.1088/0004-637X/705/1/936)

- Bouwens, R. J., Illingworth, G. D., Oesch, P. A., et al. 2014, *ApJ*, 793, 115, doi: [10.1088/0004-637X/793/2/115](https://doi.org/10.1088/0004-637X/793/2/115)
- Brammer, G. B., van Dokkum, P. G., & Coppi, P. 2008, *ApJ*, 686, 1503, doi: [10.1086/591786](https://doi.org/10.1086/591786)
- Breeveld, A. A., Curran, P. A., Hoversten, E. A., et al. 2010, *MNRAS*, 406, 1687, doi: [10.1111/j.1365-2966.2010.16832.x](https://doi.org/10.1111/j.1365-2966.2010.16832.x)
- Brown, P. J., Roming, P. W. A., Milne, P., et al. 2010, *ApJ*, 721, 1608, doi: [10.1088/0004-637X/721/2/1608](https://doi.org/10.1088/0004-637X/721/2/1608)
- Calzetti, D. 2013, in *Secular Evolution of Galaxies*, ed. J. Falcón-Barroso & J. H. Knapen, 419, doi: [10.48550/arXiv.1208.2997](https://doi.org/10.48550/arXiv.1208.2997)
- Calzetti, D., Armus, L., Bohlin, R. C., et al. 2000, *ApJ*, 533, 682, doi: [10.1086/308692](https://doi.org/10.1086/308692)
- Calzetti, D., Kinney, A. L., & Storchi-Bergmann, T. 1994, *ApJ*, 429, 582, doi: [10.1086/174346](https://doi.org/10.1086/174346)
- Capak, P., Cowie, L. L., Hu, E. M., et al. 2004, *AJ*, 127, 180, doi: [10.1086/380611](https://doi.org/10.1086/380611)
- Casey, C. M., Scoville, N. Z., Sanders, D. B., et al. 2014, *ApJ*, 796, 95, doi: [10.1088/0004-637X/796/2/95](https://doi.org/10.1088/0004-637X/796/2/95)
- Charlot, S., & Fall, S. M. 2000, *ApJ*, 539, 718, doi: [10.1086/309250](https://doi.org/10.1086/309250)
- Ciardullo, R., Gronwall, C., Adams, J. J., et al. 2013, *ApJ*, 769, 83, doi: [10.1088/0004-637X/769/1/83](https://doi.org/10.1088/0004-637X/769/1/83)
- Cohen, J. G., Hogg, D. W., Blandford, R., et al. 2000, *ApJ*, 538, 29, doi: [10.1086/309096](https://doi.org/10.1086/309096)
- Conroy, C. 2013, *ARA&A*, 51, 393, doi: [10.1146/annurev-astro-082812-141017](https://doi.org/10.1146/annurev-astro-082812-141017)
- Curtis-Lake, E., Carniani, S., Cameron, A., et al. 2023, *Nature Astronomy*, doi: [10.1038/s41550-023-01918-w](https://doi.org/10.1038/s41550-023-01918-w)
- Declair, M., De Looze, I., Boquien, M., et al. 2019, *MNRAS*, 486, 743, doi: [10.1093/mnras/stz805](https://doi.org/10.1093/mnras/stz805)
- Eddington, A. S. 1913, *MNRAS*, 73, 359, doi: [10.1093/mnras/73.5.359](https://doi.org/10.1093/mnras/73.5.359)
- Elbaz, D., Dickinson, M., Hwang, H. S., et al. 2011, *A&A*, 533, A119, doi: [10.1051/0004-6361/201117239](https://doi.org/10.1051/0004-6361/201117239)
- Finkelstein, S. L., Papovich, C., Salmon, B., et al. 2012, *ApJ*, 756, 164, doi: [10.1088/0004-637X/756/2/164](https://doi.org/10.1088/0004-637X/756/2/164)
- Fitzpatrick, E. L. 1999, *PASP*, 111, 63, doi: [10.1086/316293](https://doi.org/10.1086/316293)
- Fleming, D. E. B., Harris, W. E., Pritchett, C. J., & Hanes, D. A. 1995, *AJ*, 109, 1044, doi: [10.1086/117340](https://doi.org/10.1086/117340)
- Foreman-Mackey, D. 2016, *The Journal of Open Source Software*, 1, 24, doi: [10.21105/joss.00024](https://doi.org/10.21105/joss.00024)
- Foreman-Mackey, D., Hogg, D. W., Lang, D., & Goodman, J. 2013, *PASP*, 125, 306, doi: [10.1086/670067](https://doi.org/10.1086/670067)
- Galametz, A., Grazian, A., Fontana, A., et al. 2013, *ApJS*, 206, 10, doi: [10.1088/0067-0049/206/2/10](https://doi.org/10.1088/0067-0049/206/2/10)
- Gehrels, N. 1986, *ApJ*, 303, 336, doi: [10.1086/164079](https://doi.org/10.1086/164079)
- Gehrels, N., Chincarini, G., Giommi, P., et al. 2004, *ApJ*, 611, 1005, doi: [10.1086/422091](https://doi.org/10.1086/422091)
- Giavalisco, M., Ferguson, H. C., Koekemoer, A. M., et al. 2004, *ApJL*, 600, L93, doi: [10.1086/379232](https://doi.org/10.1086/379232)
- Gordon, K. D., Clayton, G. C., Misselt, K. A., Landolt, A. U., & Wolff, M. J. 2003, *ApJ*, 594, 279, doi: [10.1086/376774](https://doi.org/10.1086/376774)
- Grogin, N. A., Kocevski, D. D., Faber, S. M., et al. 2011, *ApJS*, 197, 35, doi: [10.1088/0067-0049/197/2/35](https://doi.org/10.1088/0067-0049/197/2/35)
- Guo, Y., Ferguson, H. C., Giavalisco, M., et al. 2013, *ApJS*, 207, 24, doi: [10.1088/0067-0049/207/2/24](https://doi.org/10.1088/0067-0049/207/2/24)
- Hagen, L. M. Z., Hoversten, E. A., Gronwall, C., et al. 2015, *ApJ*, 808, 178, doi: [10.1088/0004-637X/808/2/178](https://doi.org/10.1088/0004-637X/808/2/178)
- Hao, C.-N., Kennicutt, R. C., Johnson, B. D., et al. 2011, *ApJ*, 741, 124, doi: [10.1088/0004-637X/741/2/124](https://doi.org/10.1088/0004-637X/741/2/124)
- Hoversten, E. A., Gronwall, C., Vanden Berk, D. E., et al. 2009, *ApJ*, 705, 1462, doi: [10.1088/0004-637X/705/2/1462](https://doi.org/10.1088/0004-637X/705/2/1462)
- Hsu, L.-T., Lin, L., Dickinson, M., et al. 2019, *ApJ*, 871, 233, doi: [10.3847/1538-4357/aaf9a7](https://doi.org/10.3847/1538-4357/aaf9a7)
- Illingworth, G. D., Magee, D., Oesch, P. A., et al. 2013, *ApJS*, 209, 6, doi: [10.1088/0067-0049/209/1/6](https://doi.org/10.1088/0067-0049/209/1/6)
- Keenan, R. C., Trouille, L., Barger, A. J., Cowie, L. L., & Wang, W. H. 2010, *ApJS*, 186, 94, doi: [10.1088/0067-0049/186/1/94](https://doi.org/10.1088/0067-0049/186/1/94)
- Kennicutt, Robert C., J. 1998, *ARA&A*, 36, 189, doi: [10.1146/annurev.astro.36.1.189](https://doi.org/10.1146/annurev.astro.36.1.189)
- Kennicutt, R. C., & Evans, N. J. 2012, *ARA&A*, 50, 531, doi: [10.1146/annurev-astro-081811-125610](https://doi.org/10.1146/annurev-astro-081811-125610)
- Koekemoer, A. M., Faber, S. M., Ferguson, H. C., et al. 2011, *ApJS*, 197, 36, doi: [10.1088/0067-0049/197/2/36](https://doi.org/10.1088/0067-0049/197/2/36)
- Kong, X., Charlot, S., Brinchmann, J., & Fall, S. M. 2004, *MNRAS*, 349, 769, doi: [10.1111/j.1365-2966.2004.07556.x](https://doi.org/10.1111/j.1365-2966.2004.07556.x)
- Kron, R. G. 1980, *ApJS*, 43, 305, doi: [10.1086/190669](https://doi.org/10.1086/190669)
- Kumar, A., Ghosh, S. K., Hutchings, J., et al. 2012, in *Society of Photo-Optical Instrumentation Engineers (SPIE) Conference Series*, Vol. 8443, *Space Telescopes and Instrumentation 2012: Ultraviolet to Gamma Ray*, ed. T. Takahashi, S. S. Murray, & J.-W. A. den Herder, 84431N, doi: [10.1117/12.924507](https://doi.org/10.1117/12.924507)
- Kurczynski, P., Gawiser, E., Rafelski, M., et al. 2014, *ApJL*, 793, L5, doi: [10.1088/2041-8205/793/1/L5](https://doi.org/10.1088/2041-8205/793/1/L5)
- Labbé, I., van Dokkum, P., Nelson, E., et al. 2023, *Nature*, 616, 266, doi: [10.1038/s41586-023-05786-2](https://doi.org/10.1038/s41586-023-05786-2)
- Leja, J., Johnson, B. D., Conroy, C., et al. 2019, *ApJ*, 877, 140, doi: [10.3847/1538-4357/ab1d5a](https://doi.org/10.3847/1538-4357/ab1d5a)
- Ly, C., Malkan, M. A., Treu, T., et al. 2009, *ApJ*, 697, 1410, doi: [10.1088/0004-637X/697/2/1410](https://doi.org/10.1088/0004-637X/697/2/1410)
- Madau, P., & Dickinson, M. 2014, *ARA&A*, 52, 415, doi: [10.1146/annurev-astro-081811-125615](https://doi.org/10.1146/annurev-astro-081811-125615)

- Markov, V., Gallerani, S., Ferrara, A., et al. 2024, arXiv e-prints, arXiv:2402.05996, doi: [10.48550/arXiv.2402.05996](https://doi.org/10.48550/arXiv.2402.05996)
- Mason, K. O., Breeveld, A., Much, R., et al. 2001, *A&A*, 365, L36, doi: [10.1051/0004-6361:20000044](https://doi.org/10.1051/0004-6361:20000044)
- McQuinn, K. B. W., Skillman, E. D., Dolphin, A. E., & Mitchell, N. P. 2015, *ApJ*, 808, 109, doi: [10.1088/0004-637X/808/2/109](https://doi.org/10.1088/0004-637X/808/2/109)
- Meurer, G. R., Heckman, T. M., & Calzetti, D. 1999, *ApJ*, 521, 64, doi: [10.1086/307523](https://doi.org/10.1086/307523)
- Momcheva, I. G., Brammer, G. B., van Dokkum, P. G., et al. 2016, *ApJS*, 225, 27, doi: [10.3847/0067-0049/225/2/27](https://doi.org/10.3847/0067-0049/225/2/27)
- Mondal, C., Saha, K., Windhorst, R. A., & Jansen, R. A. 2023a, *ApJ*, 946, 90, doi: [10.3847/1538-4357/acc110](https://doi.org/10.3847/1538-4357/acc110)
- Mondal, C., Saha, K., Bhattacharya, S., et al. 2023b, *ApJS*, 264, 40, doi: [10.3847/1538-4365/aca7c4](https://doi.org/10.3847/1538-4365/aca7c4)
- Moutard, T., Sawicki, M., Arnouts, S., et al. 2020, *MNRAS*, 494, 1894, doi: [10.1093/mnras/staa706](https://doi.org/10.1093/mnras/staa706)
- Murphy, E. J., Condon, J. J., Schinnerer, E., et al. 2011, *ApJ*, 737, 67, doi: [10.1088/0004-637X/737/2/67](https://doi.org/10.1088/0004-637X/737/2/67)
- Narayanan, D., Conroy, C., Davé, R., Johnson, B. D., & Popping, G. 2018a, *ApJ*, 869, 70, doi: [10.3847/1538-4357/aaed25](https://doi.org/10.3847/1538-4357/aaed25)
- Narayanan, D., Davé, R., Johnson, B. D., et al. 2018b, *MNRAS*, 474, 1718, doi: [10.1093/mnras/stx2860](https://doi.org/10.1093/mnras/stx2860)
- Oesch, P. A., Bouwens, R. J., Carollo, C. M., et al. 2010, *ApJL*, 725, L150, doi: [10.1088/2041-8205/725/2/L150](https://doi.org/10.1088/2041-8205/725/2/L150)
- Oesch, P. A., Montes, M., Reddy, N., et al. 2018, *ApJS*, 237, 12, doi: [10.3847/1538-4365/aacb30](https://doi.org/10.3847/1538-4365/aacb30)
- Oke, J. B., & Gunn, J. E. 1983, *ApJ*, 266, 713, doi: [10.1086/160817](https://doi.org/10.1086/160817)
- Overzier, R. A., Heckman, T. M., Wang, J., et al. 2011, *ApJL*, 726, L7, doi: [10.1088/2041-8205/726/1/L7](https://doi.org/10.1088/2041-8205/726/1/L7)
- Page, M. J., Dwelly, T., McHardy, I., et al. 2021, *MNRAS*, 506, 473, doi: [10.1093/mnras/stab1638](https://doi.org/10.1093/mnras/stab1638)
- Poole, T. S., Breeveld, A. A., Page, M. J., et al. 2008, *MNRAS*, 383, 627, doi: [10.1111/j.1365-2966.2007.12563.x](https://doi.org/10.1111/j.1365-2966.2007.12563.x)
- Reddy, N. A., Steidel, C. C., Pettini, M., et al. 2008, *ApJS*, 175, 48, doi: [10.1086/521105](https://doi.org/10.1086/521105)
- Reddy, N. A., Oesch, P. A., Bouwens, R. J., et al. 2018, *ApJ*, 853, 56, doi: [10.3847/1538-4357/aaa3e7](https://doi.org/10.3847/1538-4357/aaa3e7)
- Robertson, B. E., Tacchella, S., Johnson, B. D., et al. 2023, *Nature Astronomy*, doi: [10.1038/s41550-023-01921-1](https://doi.org/10.1038/s41550-023-01921-1)
- Robitaille, T., Ginsburg, A., Mumford, S., et al. 2023, *astropy/reproject: v0.10.0, v0.10.0*, Zenodo, doi: [10.5281/zenodo.7584411](https://doi.org/10.5281/zenodo.7584411)
- Roming, P. W. A., Kennedy, T. E., Mason, K. O., et al. 2005, *SSRv*, 120, 95, doi: [10.1007/s11214-005-5095-4](https://doi.org/10.1007/s11214-005-5095-4)
- Salim, S., & Boquien, M. 2019, *ApJ*, 872, 23, doi: [10.3847/1538-4357/aaf88a](https://doi.org/10.3847/1538-4357/aaf88a)
- Salim, S., Boquien, M., & Lee, J. C. 2018, *ApJ*, 859, 11, doi: [10.3847/1538-4357/aabf3c](https://doi.org/10.3847/1538-4357/aabf3c)
- Salvato, M., Ilbert, O., & Hoyle, B. 2019, *Nature Astronomy*, 3, 212, doi: [10.1038/s41550-018-0478-0](https://doi.org/10.1038/s41550-018-0478-0)
- Schechter, P. 1976, *ApJ*, 203, 297, doi: [10.1086/154079](https://doi.org/10.1086/154079)
- Schiminovich, D., Ilbert, O., Arnouts, S., et al. 2005, *ApJL*, 619, L47, doi: [10.1086/427077](https://doi.org/10.1086/427077)
- Schlafly, E. F., & Finkbeiner, D. P. 2011, *ApJ*, 737, 103, doi: [10.1088/0004-637X/737/2/103](https://doi.org/10.1088/0004-637X/737/2/103)
- Schlegel, D. J., Finkbeiner, D. P., & Davis, M. 1998, *ApJ*, 500, 525, doi: [10.1086/305772](https://doi.org/10.1086/305772)
- Schmidt, M. 1968, *ApJ*, 151, 393, doi: [10.1086/149446](https://doi.org/10.1086/149446)
- Sharma, M., Page, M. J., & Breeveld, A. A. 2022a, *MNRAS*, 511, 4882, doi: [10.1093/mnras/stac356](https://doi.org/10.1093/mnras/stac356)
- Sharma, M., Page, M. J., Ferreras, I., & Breeveld, A. A. 2022b, arXiv e-prints, arXiv:2212.00215, doi: [10.48550/arXiv.2212.00215](https://doi.org/10.48550/arXiv.2212.00215)
- Sharma, M., Page, M. J., Symeonidis, M., & Ferreras, I. 2024, *MNRAS*, 528, 1997, doi: [10.1093/mnras/stae135](https://doi.org/10.1093/mnras/stae135)
- Shivaei, I., Reddy, N., Rieke, G., et al. 2020, *ApJ*, 899, 117, doi: [10.3847/1538-4357/aba35e](https://doi.org/10.3847/1538-4357/aba35e)
- Siegel, M. H., Porterfield, B. L., Linevsky, J. S., et al. 2014, *AJ*, 148, 131, doi: [10.1088/0004-6256/148/6/131](https://doi.org/10.1088/0004-6256/148/6/131)
- Skelton, R. E., Whitaker, K. E., Momcheva, I. G., et al. 2014, *ApJS*, 214, 24, doi: [10.1088/0067-0049/214/2/24](https://doi.org/10.1088/0067-0049/214/2/24)
- Smail, I., Hogg, D. W., Yan, L., & Cohen, J. G. 1995, *ApJL*, 449, L105, doi: [10.1086/309647](https://doi.org/10.1086/309647)
- Somerville, R. S., Lee, K., Ferguson, H. C., et al. 2004, *ApJL*, 600, L171, doi: [10.1086/378628](https://doi.org/10.1086/378628)
- Sun, L., Wang, X., Teplitz, H. I., et al. 2023, arXiv e-prints, arXiv:2311.15664, doi: [10.48550/arXiv.2311.15664](https://doi.org/10.48550/arXiv.2311.15664)
- Takeuchi, T. T., Yuan, F.-T., Ikeyama, A., Murata, K. L., & Inoue, A. K. 2012, *ApJ*, 755, 144, doi: [10.1088/0004-637X/755/2/144](https://doi.org/10.1088/0004-637X/755/2/144)
- Tandon, S. N., Subramaniam, A., Girish, V., et al. 2017, *AJ*, 154, 128, doi: [10.3847/1538-3881/aa8451](https://doi.org/10.3847/1538-3881/aa8451)
- Teplitz, H. I., Siana, B., Brown, T. M., et al. 2006, *AJ*, 132, 853, doi: [10.1086/505685](https://doi.org/10.1086/505685)
- Trenti, M., & Stiavelli, M. 2008, *ApJ*, 676, 767, doi: [10.1086/528674](https://doi.org/10.1086/528674)
- Walcher, J., Groves, B., Budavári, T., & Dale, D. 2011, *Ap&SS*, 331, 1, doi: [10.1007/s10509-010-0458-z](https://doi.org/10.1007/s10509-010-0458-z)
- Wang, W.-H., Cowie, L. L., Barger, A. J., Keenan, R. C., & Ting, H.-C. 2010, *ApJS*, 187, 251, doi: [10.1088/0067-0049/187/1/251](https://doi.org/10.1088/0067-0049/187/1/251)
- Wang, X., Teplitz, H. I., Sun, L., et al. 2024, *Research Notes of the American Astronomical Society*, 8, 26, doi: [10.3847/2515-5172/ad1f6f](https://doi.org/10.3847/2515-5172/ad1f6f)

Williams, R. E., Blacker, B., Dickinson, M., et al. 1996, AJ, 112, 1335, doi: [10.1086/118105](https://doi.org/10.1086/118105)

Wyder, T. K., Treyer, M. A., Milliard, B., et al. 2005, ApJL, 619, L15, doi: [10.1086/424735](https://doi.org/10.1086/424735)

Xu, C. K., Donas, J., Arnouts, S., et al. 2005, ApJL, 619, L11, doi: [10.1086/425252](https://doi.org/10.1086/425252)

Xu, C. K., Shupe, D., Buat, V., et al. 2007, ApJS, 173, 432, doi: [10.1086/516641](https://doi.org/10.1086/516641)

Xue, Y. Q., Luo, B., Brandt, W. N., et al. 2016, ApJS, 224, 15, doi: [10.3847/0067-0049/224/2/15](https://doi.org/10.3847/0067-0049/224/2/15)

Yang, G., Xue, Y. Q., Luo, B., et al. 2014, ApJS, 215, 27, doi: [10.1088/0067-0049/215/2/27](https://doi.org/10.1088/0067-0049/215/2/27)